Letter of Intent
for
the Higher Luminosity B Factory Super-KEKB

many many authors

February 9, 2004

Contents

Part I

Detector at Super-KEKB

Chapter 1

Current performace of the Belle detector

1.1 Particle Identifier

1.1.1 Framework

In the present Belle experiment, identification of charged hadrons (mainly $K^{\pm}/\pi^{\pm}$) is carried out by combining information from three subsystems; the number of photoelectrons ($N_{\mathrm{p.e.}}$) detected in threshold silica aerogel Cherenkov counters (ACC), time-of-flight (t.o.f.) measured in an array of plastic scintillation counters (TOF) and specific ionization energy loss (dE/dx) measured in the central drift chamber (CDC). Figure 1.1 shows a cross sectional view of the three detectors. A detailed description of the detectors can be found elsewhere [1].

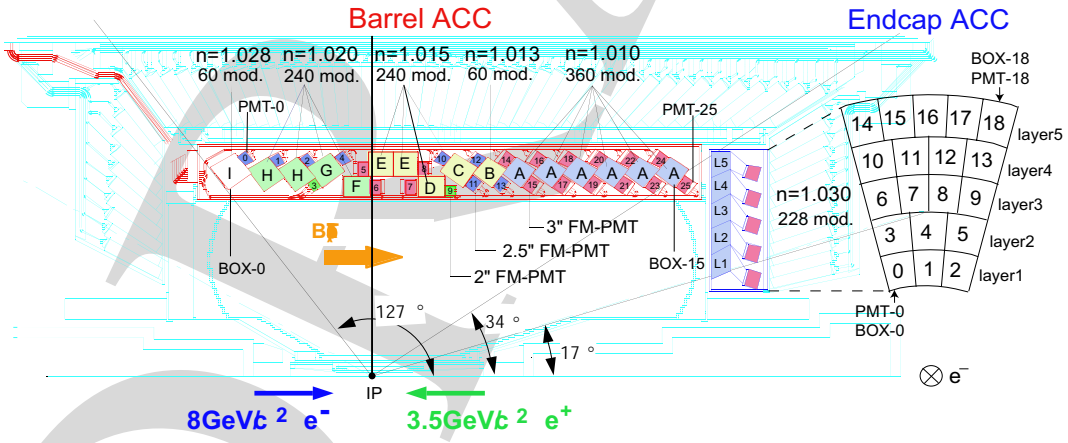

Figure 1.1: Cross-sectional view of the CDC (inner most), ACC and TOF (outer most) detectors.

The ACC system [2] is divided into the barrel and the forward endcap parts. The barrel ACC is composed of 960 counter modules, segmented into 60 cells in the ϕ direction. The endcap ACC is composed of 228 counter modules, arranged in 5 concentric layers. Each counter module is equipped with one or two fine-mesh PMT, whose diameter is either 2, 2.5 or 3 inch. The refractive index (n) of aerogels ranges from 1.010 to 1.028 for the barrel ACC, depending on the polar angular regions, to cover the momentum range from 1.2 to 3.5 GeV/c. For the endcap ACC, $n = 1.030$ has been chosen to serve for the flavor tagging. The detected light yields for

light velocity particles ranges from ~ 10 to ~ 26, depending on the type of the ACC module.

The TOF system [3] is segmented into 128 units, where each scintillator bar is 4cm thick, 6cm wide and 255cm long, and equipped with 2-inch fine-mesh PMT at both ends. The measured TOF resolution for minimum ionizing particles is about 100ps, and the system provide more than 3σ K/π separation up to 1.2 GeV/c.

The CDC [4] uses a gas mixture of 50% He and 50% C_2H_6, and has the dE/dx resolution of about 6% for Bhabha electrons. It provides K/π separation up to 0.8 GeV/c and also in the region of relativistic rise (above 2.5 GeV/c).

1.1.2 Present K/π Separation Performance

The information from the three nearly-independent measurements are combined into a single cut variable using a likelihood method. We define a $K^{\pm}$ likelihood ratio $R_K = \mathcal{L}_K/(\mathcal{L}_K + \mathcal{L}_\pi)$, where $\mathcal{L}_K(\pi)$ denotes a product of the three individual likelihoods for the $K^{\pm}(\pi^{\pm})$ mesons. Probability density functions (PDFs) for $N_{\mathrm{p.e.}}$ are obtained from a well-tuned GEANT-based Monte Carlo simulation, while those for t.o.f. and dE/dx are given in Gaussian forms, each shape deduced from data. Figure 1.2 shows the efficiency (ϵ) and misidentification rate (f) for the $K^{\pm}$ identification, measured with $D^{*+} \to D^0(\to K^-\pi^+)\pi^+$ calibration data, as a function of the track momentum in the laboratory frame (a nominal cut $R_K > 0.6$ is applied). The achieved kaon identification efficiency is about 85% with the misidentification rate lower than 10%, in the momentum region up to 4 GeV/c.

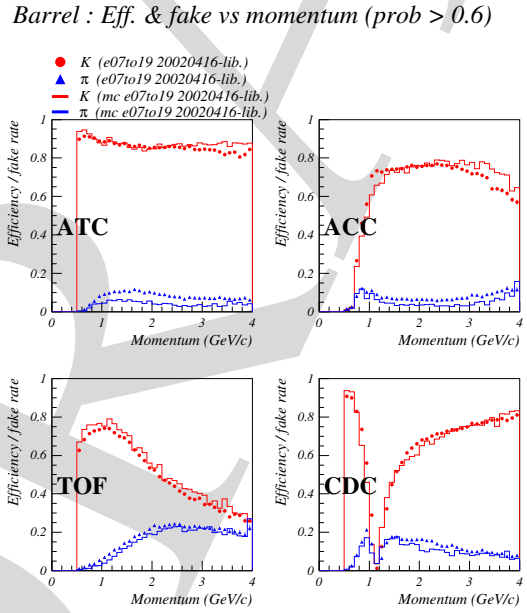

Figure 1.2: Efficiency and misidentification rate for the $K^{\pm}$ (right) identification at the Belle experiment as a function of the track momentum in the laboratory frame.

The inefficiency and misidentification arises from some sources. For example, δ-ray emitted either from the ACC counter box material or the aerogel radiator and also scintillation lights from a diffusive reflector can cause $K^{\pm} \to \pi^{\pm}$ misidentification. The inefficiency arises also from the geometrical gap between the detector modules. There is contribution also from direct particle hits on a PMT glass window, where huge $N_{\mathrm{p.e.}}$ is produced and the identification is no longer possible.

1.1.3 Disadvantage of the Present PID System

The present Belle PID system works effectively for measurements of many B decay channels. However, there are some disadvantages, that motivate the future upgrade, as discussed in detail later.

K/π separation While the present system based on the threshold Cherenkov device has advantage for robust and stable operation, the achieved K/π separation may not be enough for some important channels at the Super-KEKB/Belle experiment. A Cherenkov system based on ring imaging technology, as used in the BaBar experiment, would be a promising approach for improvement. In the BaBar experiment, $K^{\pm}/\pi^{\pm}$ separation is carried out mostly by using the Detector-of-Internally-Reflected-Cherenkov-light (DIRC). The DIRC counter consists of long quartz bars facing to a water-filled expansion region, called the standoff box. Approximately 10,000 photomultiplier tubes are located on the wall of the standoff box to reconstruct a ring image. Table 1.1 compares the performance for the kaon identification between Belle and BaBar, based on numbers referred from [1] and [5], although they cannot be directly compared.

Table 1.1: Comparison of the $K^{\pm}$ and $\pi^{\pm}$ identification performance at the Belle (upper row) and BaBar (lower row) experiments.

p [GeV/c]	ϵ_K [%]	f_π [%]	ϵ_π [%]	f_K [%]
1.80–2.00	85.4 ± 0.3	10.2 ± 0.3	86.5 ± 0.3	10.5 ± 0.3
1.75–2.00	~ 99	~ 2	—	—
3.00–3.50	83.8 ± 0.3	7.2 ± 0.2	89.5 ± 0.2	11.2 ± 0.2
3.25–3.50	~ 87	~ 11	—	—

Angular coverage for the high momentum PID In the present system, the forward endcap part functions only for the flavor tagging, and it does not provide meaningful K/π separation above 2.0 GeV/c. In this angular region, the track momentum from two-body decays of the B meson reach slightly above 4GeV/c. If based on a threshold device, aerogels with refractive index of about 1.007 was desired to cover the momentum region of interest. However, it was too difficult to develop such a system at the time of construction of the present Belle.

Material thickness Another disadvantage of the present system is an amount of materials, that affect the performance of the electromagnetic calorimeter located outside. The material thickness in radiation length of the present system is about $\sim *\%$ in total, $\sim *\%$ from ACC and $\sim *\%$ from TOF scintillator. The major contribution to the ACC material comes from the fine-mesh PMT's.

1.1.4 Background situation

The background level for the present Belle PID systm was evaluated using the real beam data taken in 2003 and Table 1.2 summarizes the background situation with an assumption of 10 A total current.

As for the TOF system, the measured PMT single rate is 44 kHz with 20 nsec full width signal in typical runs, where the sum of HER and LER current is about 2.5A. Then, assuming a

detector	hit rate(kHz)	dead time(%)
TOF	170	12
EACC(1st layer)	18	1.3
EACC(5th layer)	6	0.4

Table 1.2: The hit rate estimated assuming total current is 10 A. The dead time shown here is limited by the present readout specifications.

linear dependence, it is exptrapolated to 170 kHz for 10 A current. This indicates the inefficiency of the TOF counter can go up to 12 % in case that the present MQT and the time stretcher board are applied. Therefore, the present TOF system does not work, unless we develop a detector with finer segmentation or a fast readout with signal processing time of less than 100ns.

As for the ACC system, Figure 1.3 shows the background rate as a function of the EACC layer number, for four different sectors in the ϕ direction. The hit rate is the maximum 2.6 kHz at the innermost layer at r = 500 mm, and decreases to 1.0 kHz at the outermost layer at r = 1030 mm. The hit rate has also a clear ϕ dependence, as shown in the figure, and is the lowest in the sector #10, located at the bottom part of the detector. This can be understood because there is massive material in front of the bottom part of the EACC, which is the supporting system of the QCS magnets.

The current dependence of the hit rate for each layer is plotted in figure 1.3, where the horizontal axis stands for a sum of LER and HER currents. Assuming a linear dependence again, one can extrapolate into 18 kHz for 10 A and 39 kHz for 20 A for the innermost layer. Note that hit rate for the barrel ACC, located just inside of the TOF counter, is almost similar to that observed at the outermost EACC layer, which is evaluated to be 6 kHz for 10 A. The intrinsic dead time for high current enviroment with the present MQT readout system can be estimated to be 1.3 % dead time for 10 A.

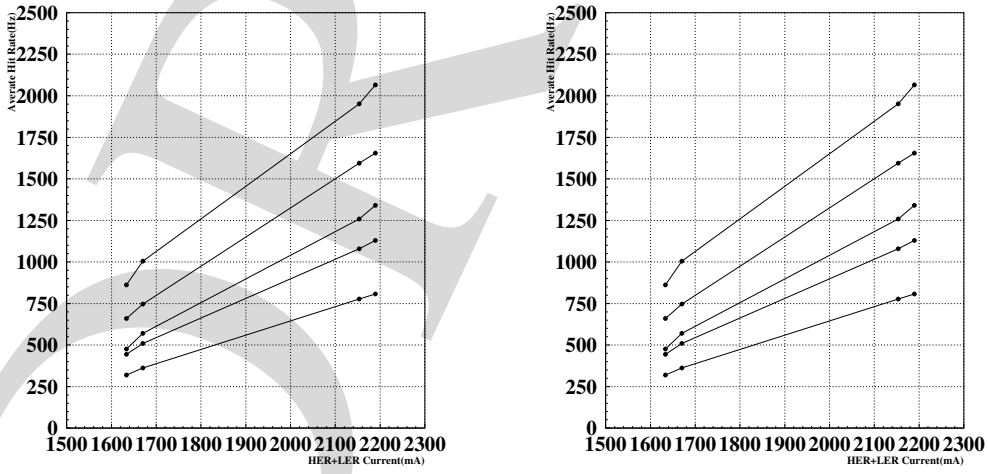

Figure 1.3: Layer dependence of the EACC hit rates for 4 sectors in a typical run (left), and EACC hit rates as a function of a sum of HER and LER currents (right).

References

[1] A. Abashian *et al.* (Belle Collaboration), Nucl. Inst. Meth. A **479**, 117 (2002).

[2] T.Iijima *et al.*, *Nucl. Instrum. Methods* A **379**, 457 (1996); T.Iijima *et al.*, *Nucl. Instrum. Methods* A **387**, 64 (1997); R.Suda *et al.*, *Nucl. Instrum. Methods* A **406**, 213 (1998), M.H.R.Khan *et al.*, *Nucl. Instrum. Methods* A **413**, 201 (1998); T.Sumiyoshi *et al.*, *Nucl. Instrum. Methods* A **433**, 385 (1999).

[3] H.Kichimi *et al.*, Proceedings of the 7th International Conference on Instrumentation for Colliding Beam Physics, Hamamatsu, Japan, November 15-19, 1999, submitted to *Nucl. Instrum. Methods* A; H.Kichimi *et al.*, *Nucl. Instrum. Methods* A **325**, 451 (1993).

[4] S.Uno, *Nucl. Instrum. Methods* A **379**, 421 (1996); K.Emi *et al.*, *Nucl. Instrum. Methods* A **379**, 225 (1996); S.Uno *et al.*, *Nucl. Instrum. Methods* A **330**, 55 (1993).

[5] B. Aubert *et al.* (BaBar Collaboration), Nucl. Inst. Meth. A **479**, 54 (2002); J. Schwiening, Nucl. Inst. Meth. A **502**, 67 (2003); See the following URL for more recent information, http://www.slac.stanford.edu/BFROOT/www/Detector/DIRC.

Chapter 2

Conditions and requirements for the detector at super-KEKB

2.1 Requirements for Particle Identifier

2.1.1 Impact of PID Improvement on Physics Reach

Particle identification, especially the K/π separation, plays a crucial role in the B-factory experiments. This situation will remain unchanged also at the Super-KEKB/Belle experiment, which aims at precise test of Kobayashi-Maskawa scheme for the CP violation and search for new physics effects in B meson decays. For the precise measurement of the ϕ_1, ϕ_2 and ϕ_3 angles, the particle identification is essential in the following aspects.

- Flavor tagging in any type of time-dependent CP asymmetry measurements.
- Reconstruction of charmless two-body decays such as $B \to \pi\pi$, $K\pi$, ϕK and $\eta' K$.
- Reconstruction of $B \to DK$ and $D\pi$ decays.

Moreover, in search for new physics effects in B meson decays, importance of the K/π separation increases. One such example is;

- $b \to s\gamma$ and $d\gamma$ decays; it is noted here that these two decays have only weak kinematical separation and also that the branching fraction of $b \to d\gamma$ is expected to be at least an order of magnitude lower than the $b \to s\gamma$.

Another aspect to be considered is the μ/π separation in the momentum region below 0.7 GeV/c, where the KLM detector cannot be used for the muon identification. A typical example is;

- Forward-backward asymmetry A_{FB} in $b \to s\ell^+\ell^-$.

In order to meet these requirements, the upgraded PID system should have more than 4 σ K/π separation in the wide momentum region up to 4 GeV/c. Such system would provide similar μ/π separation up to 0.7 GeV/c.

In following, impacts of PID improvement are demonstrated for some bench-mark physics channels.

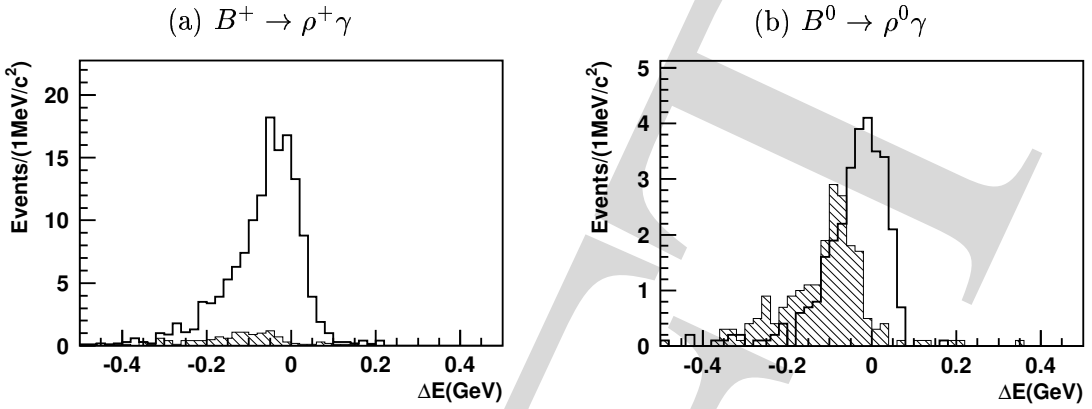

Figure 2.1: ΔE distribution for (a) $B^+ \to \rho^+\gamma$ and (b) $B^0 \to \rho^0\gamma$. Open histograms show the $B \to \rho\gamma$ signal, while shaded histograms show the contributions from $B \to K^*(892)\gamma$ assuming 3% of kaon-to-pion misidentification rate. Histograms are scaled to 5 ab^{-1}.

Measurement of $B \to \rho\gamma$

This mode proceeds through the $b \to d\gamma$ process, and is useful for the measurement of $|V_{td}|$. $B^+ \to \rho^+\gamma$ can be also used to measure the CP asymmetry, which is expected to be large in the SM. The time-dependent asymmetry of $B^0 \to \rho^0\gamma$ is expected to be small in the SM, but can be large in some non-SM models. Hence, this mode is a sensitive probe for new Physics.

However, $B \to \rho\gamma$ decays suffer large background from $B \to K^*\gamma$ decays by mis-identifying a kaon from K^* as a pion, because $b \to d\gamma$ is suppressed by the factor of $|V_{td}/V_{ts}|^2 < 0.06$ compared to $b \to s\gamma$. The branching fraction of $B \to \rho\gamma$ is predicted to be $(0.85 \pm 0.30 \pm 0.10) \times 10^{-6}$ and $(0.49 \pm 0.17 \pm 0.04) \times 10^{-6}$ for the charged and neutral mode [1], while that of $B \to K^*\gamma$ is around 4×10^{-5}. Therefore, the separation of kaons and pions is a critical issue for the study of $B \to \rho\gamma$.

The effect of the PID to the experimental sensitivity is studied using simple FSIM program. The reconstruction of $B \to \rho\gamma$ is performed for the $B \to K^*\gamma$ and $B \to \rho\gamma$ MC samples. The selection criteria are based on the present analysis at Belle: we apply π^0/η veto, $|M(\pi\pi) - M_\rho| < 200$ MeV/c^2 and $|M(K\pi) - M_{K^*}| > 80$ MeV/c^2, where M_ρ (M_{K^*}) is the nominal $\rho(K^*)$ mass and $M(K\pi)$ is the invariant mass of the two pions assuming kaon mass for the higher momentum charged pion. The selection criteria for continuum background suppression are not applied. We assume 10% efficiency for this kind of selections, and scale the histograms afterward. In order to see roughly the contribution of the PID performance to the study, the π efficiency is fixed to be 90% and the mis-identification rate is varied. For simplicity, the performance is assumed to be independent of the momentum of the charged particle.

Figure 2.1 show the ΔE distributions after applying $M_{\rm bc} > 5.27$ GeV/c^2, assuming 3 % mis-identification rate. The histograms are scaled to 5 ab^{-1}, taking into account the assumed 10% efficiency for continuum background suppression. The distributions for the $B \to K^*\gamma$ are shifted by around -100 MeV because of the mass difference between kaons and pions. However, the ΔE distribution for the signal also has a large tail in the lower side mainly due to the energy leakage of the high energy photons at the calorimeter. So, this energy shift is not enough to separate $B \to \rho\gamma$ and $B \to K^*\gamma$. As seen from Fig. 2.1, 3 % mis-identification rate is still too large to separate $B^0 \to \rho^0\gamma$ events from B $to K^*\gamma$ background.

Figure 2.2 shows the relation between S/N and kaon-to-pion misidentification rate. Here,

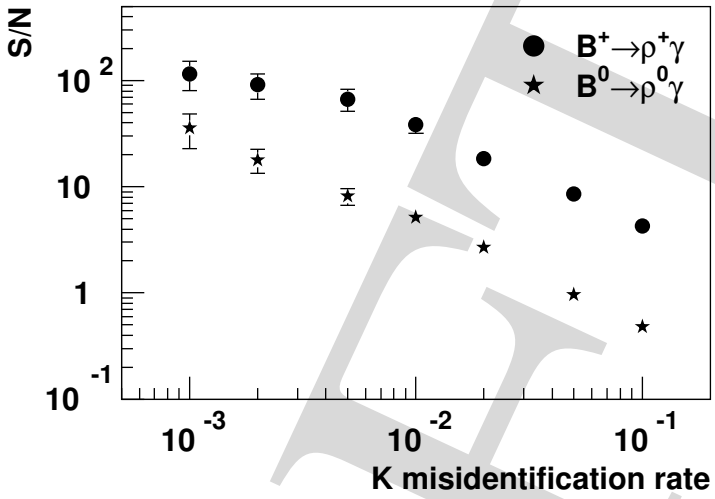

Figure 2.2: Ratio of the $B \to \rho\gamma$ signal the and $B \to K^*(892)\gamma$ background (S/N) for various kaon-to-pion misidentification rate.

S/N is the ratio of the number of $B \to \rho\gamma$ signal and $B \to K^*(892)\gamma$ background events that fall into -200 MeV/$c^2 < \Delta E < 100$ MeV/c^2. In order to make the $B \to K^*(892)\gamma$ background small enough, the misidentification rate of less than 1% ($\sim 4\sigma$ K/π separation) should be achieved.

μ/π separation for $b \to s\ell^+\ell^-$

The contribution of the PID system to the separation between muons and pions is also useful for various physics, because the KLM detector cannot identify muons with momentum less than 0.7 GeV/c^2. An example of such a physics is the $b \to s\ell\ell$ process. This process is considered to be sensitive to non-SM physics, and, in order to explore New Physics, we measure the $\hat{s}$ dependence of the branching fraction and forward-backward asymmetry $A_{\rm FB}$ both for inclusive and exclusive modes. Here, $\hat{s} = M^2(\ell^+\ell^-)/M_B^2$ (M_B is the B meson mass). Because the contribution of $c\bar{c}$ resonances such as J/ψ causes theoretical uncertainty in the region $\hat{s} \geq M_{J/\psi}^2/M_B^2$, measurement at low $\hat{s}$ region is important.

Figure 2.3 shows the $M^2(\ell^+\ell^-)$ distribution for the $B^+ \to K^+\ell^+\ell^-$ signal MC, assuming 50 ab^{-1} for various μ momentum selection. Here, muon identification efficiency is assumed to be 90% independent of the momentum. As seen from the figure, the efficiency at $M^2(\ell^+\ell^-) <$ 9 GeV/c^2 is increased as the minimum momentum of the μ selection is lowered. If we can separate muons at a low momentum region, we can increase the signal events at low $\hat{s}$ region resulting in better measurement on the branching fraction and $A_{\rm FB}$.

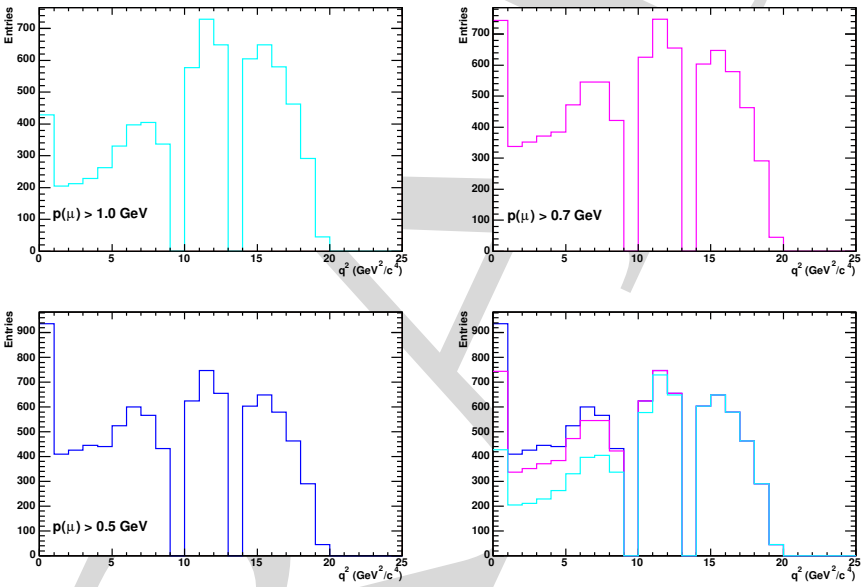

Figure 2.3: $q^2 = M^2(\ell^+\ell^-)$ distribution for $B^+ \to K^+\ell^+\ell^-$ signal MC assuming 50 ab^{-1}, for $p(\mu) > 1$ GeV/c^2, $p(\mu) > 0.7$ GeV/c^2 and $p(\mu) > 0.5$ GeV/c^2.

References

[1] A. Ali and A. Y. Parkhomenko, Eur. Phys. J. **C23**, 89 (2002).

Chapter 3

super-Belle at super-KEKB

3.1 Particle Identifier

3.1.1 Overview

Particle identification (PID), especially the K/π separation, plays a crucial role in the B-factory experiments. This situation will remain unchanged also at the Super-KEKB/Belle experiment, as discussed earlier.

We would like to upgrade the Belle PID system in order to improve the performance and meet the requirement at the Super-KEKB/Belle. The upgraded system should uncover the disadvantages of the present system, described in Section 1.1.3, and improve our physics reach, as discussed in Section 2.1. The neccessity of the improvement arises also from consideration on increasing background. Radiation hardness of detector components also have to be carefully examined.

For the improvement of the particle identification performance, it is desired to upgrade the detector with ring imaging Cherenkov counters. We propose the following two types of new detectors for upgrade of the Belle PID system;

- *Time Of Propagation (TOP) counter* for the barrel PID.
- *Proximity Focusing Aerogel RICH* for the endcap PID.

We have carried out R&D's for the two detectors in the past years. In this section, concept, design, expected performance and R&D status of these proposed detectors are present. If these detectors are realized, they will completely replace the present Belle PID detectors, ACC and TOF.

While we propose these two detectors as the baseline upgrade options, we also consider options for the barrel part, based on time-of-flight technique;

- *Tile TOF counter* aiming at $10 \sim 20$ps timing resolution, utilizing relatively small Cherenkov radiators.
- *50ps TOF counter* as upgrade of the present Belle-TOF with finer segmentation.

Idea of these backup options and some R&D status also are described in this section. In case of these TOF options, we have to consider usage in combination with the present Belle-ACC system in order to cover the high momentum region.

3.1.2 TOP counter (barrel)

Introduction

The TOP counter [1] utilizes total internal reflection of Cherenkov photons produced in a quartz bar. Figure 3.1 shows the detector principle of the TOP counter. When a charged particle passes through a quartz radiator bar, Cherenkov photons are emitted in a conical direction defined by the emission angle θ_c, and transported to the end of the bar by means of total reflection. In the case of the DIRC counter, used in the BaBar experiment [2], a ring image of the transported Cherenkov photons is magnified and projected onto a PMT array in a large stand-off. The Cherenkov emission angle θ_c is then calculated from two-dimensional hit coordinates (X-Y) of each photon. On the other hand, in case of the TOP counter, the two-dimensional information of the ring image is represented by the TOP (time of propagation) and the horizontal emission angle (Φ) of the Cherenkov photons,

$$TOP(\Phi;\theta_C) = \left(\frac{L}{v_g(\lambda)}\right) \times \frac{1}{q_z(\Phi,\theta_c)}, \tag{3.1}$$

where L is a distance which the light travels along the bar, $v_g(\lambda)$ is a group velocity of light in the quartz medium, and q_z is z-component of unit velocity vector. Since the time-of-flight (TOF) difference between two particle species from the interaction point to the detector enhances their TOP difference in most cases, TOF is appended to TOP. For instance, when 3 GeV/c K and π meson are incident on the quartz bar, $\Delta TOP \sim 75$ ps at $L = 1$ m, and $\Delta TOF \sim 50$ ps for a flight length of 1 m. Therefore, with enough photostatistics ($N_{pe} > 20$), the time measurement for each arriving photon with ~ 100 ps precision provides significant K/π separation.

In principle, the time measurement uncertainty per each detected photon (σ_{time}) arises from three major sources; 1) chromatic dispersion in photon propagation inside the quartz bar (σ_{chro}), 2) imperfectness in polishing the quartz bar (σ_{polish}), and 3) transit time spread (TTS) of the photodetector (σ_{TTS}). The chromatic dispersion arises from wavelength dependence of the group velocity of photons propagating inside the quartz bar ($v_g(\lambda)$), therefore, σ_{chro} depends on the bandwidth in the photodetection and also on the propagation distance (L). For instance, when a typical bialkali photocathode ($\lambda = 300 \sim 400$ nm) is used, σ_{chro} is estimated to be about 100 ps at $L = 1$ m.

Therefore, as in the case of the DIRC counter, good polishing accuracy of the quartz bar is required so that σ_{polish} is small enough compared to σ_{chro}. The TOP counter requires also a position sensitive photodetector with superior TTS (< 100 ps) for single photon. These are the two big challenges in the development of the TOP counter. The details of the TOP counter principle and status of our earlier development can be found in [1].

"Bar-TOP" counter

Figure 3.2 shows a schematic drawing of a TOP counter module, which is proposed for application to the Super-KEKB/Belle. The TOP module presented here is referred to as "Bar-TOP", that is different and further simplified from that in our earlier development described in [1]. It is composed of a quartz bar radiator and a photodetector array. The radiator is a well polished synthetic fused silica bar, as discussed later in Section 3.1.2. Its dimension is 2 cm in thickness and 255 cm in the length. The width is $20 \sim 40$ cm in our present consideration, and is a design parameter to be optimized taking account of the PID performance, feasibility in production and

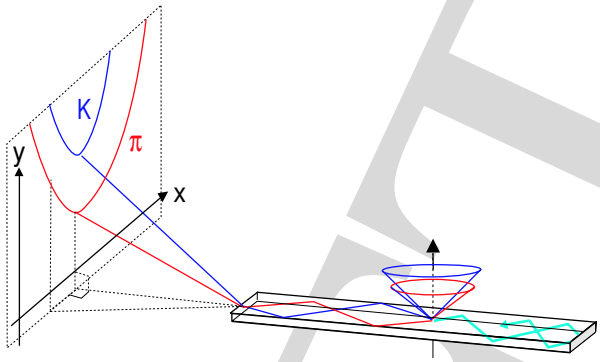

Figure 3.1: Principle of the TOP counter.

background immunity. The photodetector array is attached at the end of the bar to measure the horizontal position (X) and time of each arriving Cherenkov photons. We presently consider attach an array of multi-anode PMT's based on micro-channel-plates (MCP-PMT), each having 4 linear anodes with 5 mm pitch. More details of the photodetector are described in Section 3.1.2.

Figure 3.3 shows the relation between the X position and TOP for each detected photon. Because the X-TOP image is flipped at the side edge for several times, their relation cannot be uniquely extracted for each hit. However, enlargement of the quartz-bar width to wider than 20 cm will solve this entangled relation, as illustrated in Figure 3.3.

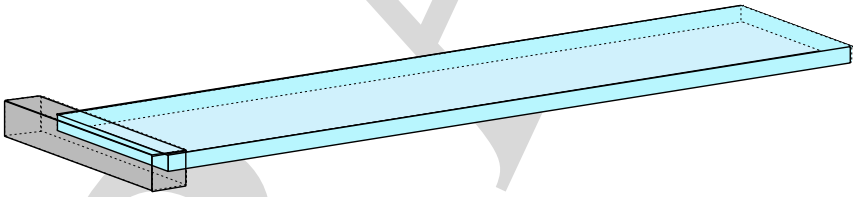

Figure 3.2: Schematic drawing of the Bar-TOP counter.

Detector Configuration in Belle

For the installation to the Belle detector, the "Bar-TOP" counter modules are arranged in a barrel-shape array. Such an array would easily fit to the barrel part of the Belle detector. Figure 3.4 shows our preliminary design of the array, where we assume that the bar width is 40 cm. In this case, the array is segmented into 18 modules, with the innermost surface located at the radial distance of 118 cm from IP. The gap between the two adjacent bars is about 1 cm, giving the dead space of approximately 3%. The required radial space is 10 cm, from r =115 to 125 cm, including the bar thickness (2 cm), sagitta (1 cm), mechanical support structure and margin for installation. The quartz bar expands in the beam direction for 255 cm, from $z = -72.5$ to 182.5 cm, to cover the polar angular region from 33.3° to 148.9°. The number of readout channels will be 60 channels per module and 1080 channels in total, in case that a 40 cm wide bar is used. The 2cm thick quartz corresponds to 16% in radiation length.

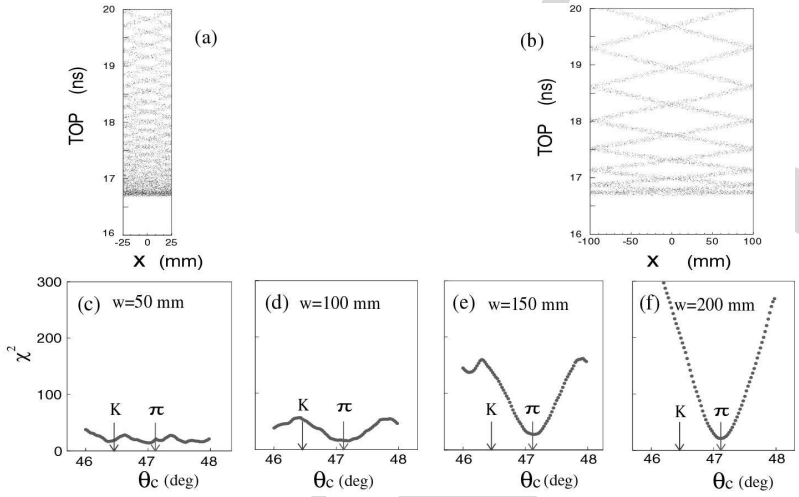

Figure 3.3: Principle of the Bar-TOP counter. X-position-vs-TOP relation and π/K separation in terms of χ^2 are shown at (a) and (c), respectively, for 50 mm-wide bar and (b) and (d) for 200 mm-wide bar. For illustration purpose, the effects of chromaticity and TTS are not included in (a) and (b), and that of TTS is not considered in (c) and (d).

Principle Confirmation with Prototype

In order to confirm the principle of the "Bar-TOP" counter, we have constructed a prototype module, as shown in Figure 3.5. The size of the quartz bar is 100 cm (length) $\times$ 20 cm (width) $\times$ 2 cm (thickness). Photodetection is made by an array of multi-anode PMT's, HPK R5900-00-L16, which has 16 channel linear anodes with 1 mm spacing. The PMT is single photon sensitive and its typical TTS is about 75 ps (σ). Figure 3.6 shows the ring image obtained with 3 GeV/c pion beams incident at the position of $L = 10$ cm. A clear X-TOP ring image is obtained.

Quartz radiator

For the quartz radiator material, synthetic fused silica would be the most appropriate choice because of long transmission length, good polishability and radiation hardness. Synthetic fused silica is available, for example, from Shin-etsu Quartz Company; their product 'SUPRASIL-P30' has a refractive index of $n = 1.47$ at a wavelength (λ) of 390 nm and a bulk transmittance of 90% at $\lambda = 250$ nm. As in the case of the DIRC counter, its surface has to be polished with a great accuracy to preserve the X-TOP relation after internal reflections of several ten times. We have tested quartz bars polished by different companies, and so far obtained satisfactory results with those polished by Okamoto Kogaku Co. in Yokohama, Japan. Table 3.1 compares polishing accuracy by two companies (bar#2 is polished by Okamoto Kogaku Co.) and the TOP resolution at $L = 2$ m, measured in the beam test of our prototype counters [1]. Figure 3.7 shows the measured timing resolution as a function of the propagation distance (L). The measured timing resolution for the quartz bar #2 is close to the limit due to the chromatic dispersion. Therefore, the contribution from the polishing accuracy to the TOP uncertainty is small enough.

[1] These measurements are carried out with prototype TOP counters with a focusing mirror, so-called "Butterfly-TOP".

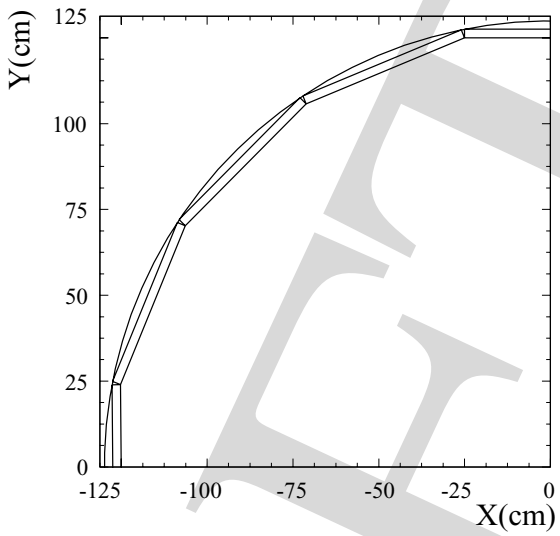

Figure 3.4: Configuration of the TOP module array in the barrel part of Belle.

Table 3.1: Comparison of polishing accuracy by two companies and the measured TOP resolution at $L = 2\,\mathrm{m}$.

	polish	figure	squareness	edge radius	time resolution
Bar #1 (old)	2 nm	5 μm	2 mrad	50 μm	300 ps
Bar #2 (new)	0.5 nm	0.6 μm	0.6 mrad	5 μm	150 ps

Photodetection

The TOP counter requires photodetectors, which can detect a single photon with; 1) good timing resolution ($< 100\,\mathrm{ps}$), 2) position resolution ($\sim 5\,\mathrm{mm}$ in one direction), 3) high quantum efficiency ($> 20\%$ at peak), 4)large effective area ($> 70\%$ per package) and 5)magnetic field immunity (up to 1.5T). Since none of photodetectors in market do not satisfy such requirement, it is necessary to develop new devices.

For this purpose, we have produced multi-anode PMT's with different dynode technologies in collaboration with Hamamatsu Photonics Co. [3]; 1) a metal-dynode PMT with 16 linear anodes (L16, R5900-00-L16), 2) a fine-mesh PMT with 24 linear anodes (L24, R6135MOD/A-L24X) and 3) a micro-channel-plate PMT (MCP-PMT) with 4 linear anodes (SL10), and investigated their characteristics. Table 3.2 compares basic performance of these devices. Among them, the MCP-PMT has been considered as the primary candidate to be used for the TOP counter because of its superior timing resolution of about 35 ps and immunity to the magnetic field.

Figure 3.8 shows a photograph and a schematic drawing of the 1st prototype of the developed 4-linear-anode MCP-PMT. The PMT has an effective area of $22\,\mathrm{mm} \times 22\,\mathrm{mm}$ in $27\,\mathrm{mm} \times 27\,\mathrm{mm}$ package, two stages of micro-channel-plates for electron amplification. Figure 3.9 shows the measured gain and TTS as a function of the magnetic field strength. We have confirmed that the developed MCP-PMT satisfies the critical performance; the gain higher than 10^6 and TTS of about 35 ps (σ) even inside the magnetic field of 1.5T. Presently, some remaining issues, such as life and high rate capability are investigated. We are also trying modification of designs to reduce cross talks and also to further improve the gain.

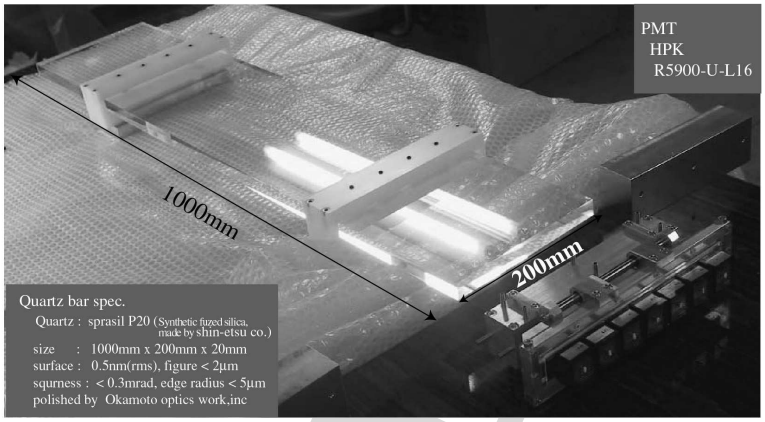

Figure 3.5: Photograph of the "Bar-TOP" prototype counter.

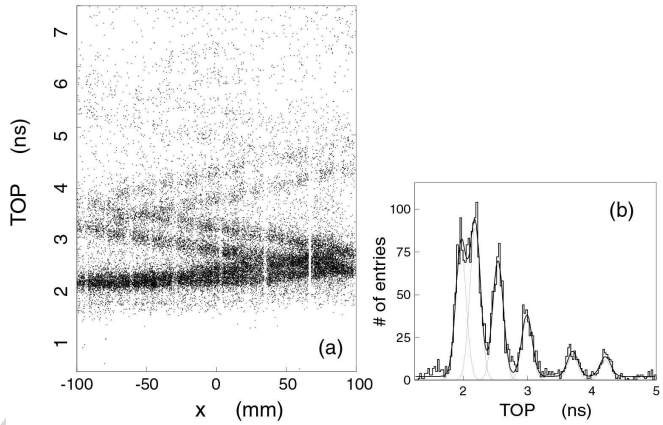

Figure 3.6: Beamtest result for the prototype counter.

Expected Performance

In an approximate form, the separation power (S) between two particle species using the TOP counter is expressed as,

$$S = \frac{\Delta T}{\sigma_{time}} \times \sqrt{N_{pe}} = \frac{\Delta TOP + \Delta TOF}{\sigma_{time}} \times \sqrt{N_{pe}} \tag{3.2}$$

Here, ΔT denotes the difference between the two particle species for the sum of TOP and TOF, N_{pe} the average number of detected photons per track and σ_{time} the single photon resolution. All of these quantities are strongly correlated with the incident position and angle of incoming particles. Therefore, PID performance depends on their polar angle, when the TOP counter is installed in the barrel part of the Belle detector.

We have performed a detailed Monte Carlo simulation to predict the performance in the Belle experiment. For production and propagation of Cherenkov photons, it takes account of chromatic dispersion effects both in the emission and propagation, and loss due to bulk absorption in quartz medium and loss at each bounce. For photodetection, it uses the measured

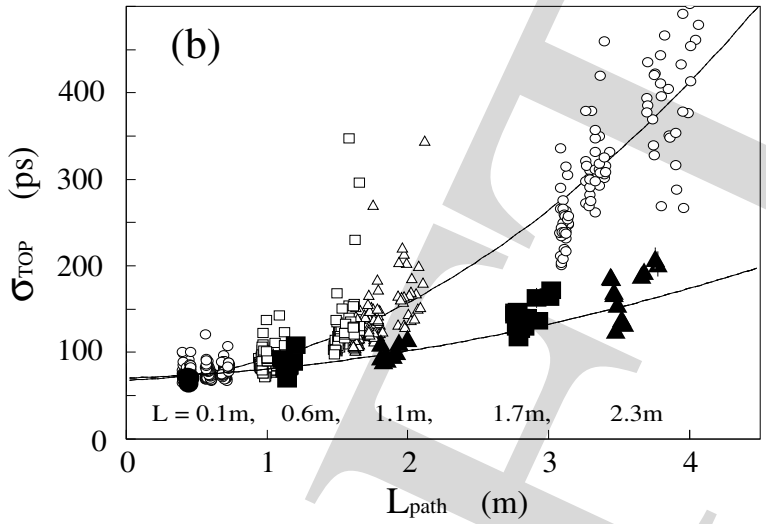

Figure 3.7: Single photon resolution as a function of the propagation distance L in beam tests of prototype counters.

Table 3.2: Comparison of PMT's with different dynodes; G(0T) stands for gain without the magnetic field, G(1.5T)/G(0T) gain reduction at 1.5T, TTS(0T/1.5T) is the TTS (σ) with the 0T/1.5T magnetic field.

Type	Dynode	Anode (pitch)	G(0T)	G(1.5T)/G(0T)	TTS (0T/1.5T)
L16	metal dynode	16 (1mm)	$\sim 10^7$	—	75ps / —
L24	fine-mesh	24 (1mm)	$\sim 10^7$	10^{-2}	100ps / 150ps
SL10	MCP	4 (5mm)	$\sim 10^6$	0.5	35ps / 35ps

performance of the 4-linear-anode MCP-PMT, such as TTS, quantum efficiency and collection efficiency, as described earlier. It also takes account of effects of background Cherenkov photons produced via interaction of primary incoming tracks with the quartz material, such as δ-ray emission and hadronic interaction, based on the GEANT framework.

Figure 3.10 shows the obtained K/π separation contour in the two-dimensional plane of the polar angle (horizontal axis) and the momentum (vertical axis) of incoming tracks. The line representing the kinematics of two-body B decays is also shown. Here the geometry of the TOP counter module is same as that shown in Figure 3.4, and the quartz bar width is taken to be 40 cm. The figure indicates that the TOP counter provides K/π separation of more than 5σ in the regime of flavor tagging below 2 GeV/c, and more than 3σ for two-body B decays.

Beam Background Issue

In the high luminosity environment at the Super-KEKB/Belle, beam-induced background is a potential problem. We have studied rate of beam-induced background hits, using the spent beam generator in the Belle Geant framework. At the present KEKB luminosity, the generator gives spent e^+/e^- beams from Bremsstrahlung and Coulomb scattering at a total rate of 13 MHz. Background particles are then generated and their interactions with the TOP counter are simulated. According to the simulation, the rate of particles entering the TOP counter is

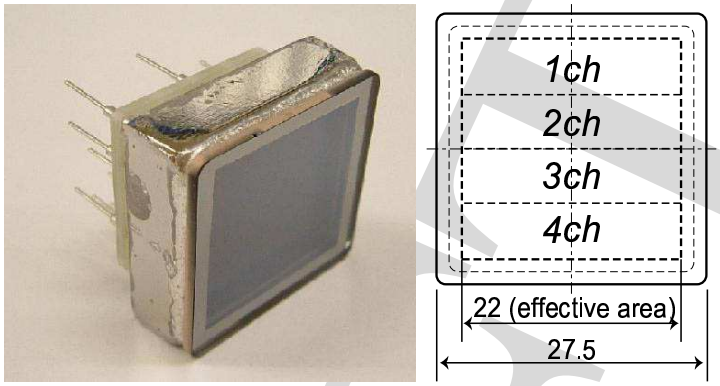

Figure 3.8: Photograph of the 1st prototype and structure of the 4-linear-anode MCP-PMT (SL10) under development.

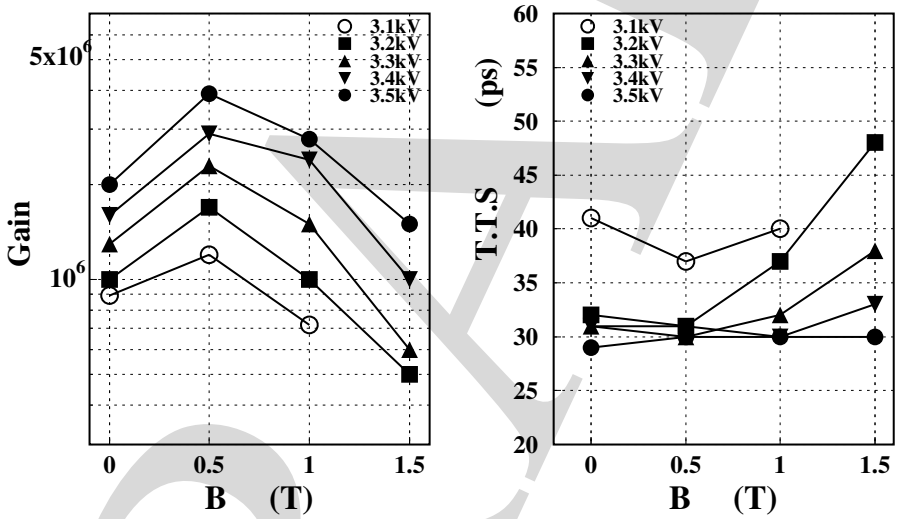

Figure 3.9: Performance of the 4-linear-anode MCP-PMT (SL10).

21 MHz (mainly photons and electrons) in the whole barrel array, and about 4% of them give hits in the photodetector [2] This converts to 45 KHz particle hits per 40 cm wide module at the present luminosity, and 900 KHz assuming 20 times higher background at the Super-KEKB. The simulation indicates that these particles leave hits in about 7 channels on the average among 60 channels in the module. Therefore, the overall detector dead time is about 1%, assuming 100 ns deadtime per hit for single PMT channel, and it is in a tolerable range. However, estimation of the beam-induced background has large uncertainties, and we need further careful studies.

[2]For calibration, the same spent beam generator and Belle detector simulation predict 400 $\sim$ 500KHz hits for the present Belle-TOF at 0.1mips threshold. The observed rate is $\sim$ 200KHz, in a good agreement with the prediction.

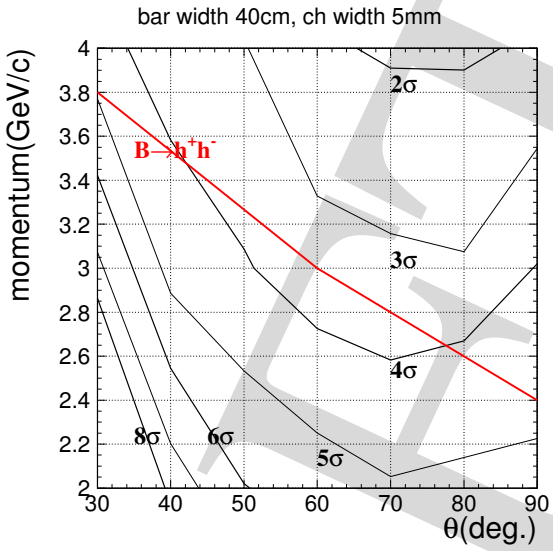

Figure 3.10: K/π separation contour in the two-dimensional plane of the polar angle (horizontal axis) and the momentum (vertical axis) of incoming tracks.

Possible Improvement

We think the above described performance is achievable with the technology at hand, and such a system would be ready for construction in time. We note here two possibilities to further improve the performance, although they require some new development.

- *Optimization of bandwidth in the photodetetion:* In the present design, the chromatic dispersion (σ_{chro}) contributes largely to the single photon resolution (σ_{time}). This can be reduced by utilizing photocathod, which is sensitive for longer wavelength region than usual bialkali photocathod. For example, GaAsP photocathod is known to be sensitive for the wavelength region of $450 \sim 650\,\mathrm{nm}$. It even has peak quantum efficiency as high as 40%, compensating enough the descrease of emitted Cherenkov photons with $1/\lambda^2$ dependence. We estimate that the $\sim 3.5\sigma K/\pi$ separation in the region around $(\theta, p) = (60^\circ, 3\mathrm{GeV}/c)$ can be improved to $\sim 6\sigma$ in this case. The critical issue for this option is the feasibility to produce a MCP-PMT, equipped with GaAsP photocathod.

- *3D imaging of Cherenkov photons:* If we measure each Cherenkov photon in three coordinates, i.e., measure the vertical emission angle in addition to (Φ, TOP), better K/π separation would be obtained. In this case, the chromatic dispersion can be corrected using correlation between the emission angle and TOP. For instance, the vertical emission angle can be measured by introducing a mirror-based focusing optics, and a two-dimensional position measurement in the photodetection. Such possibilities are discussed in [4]. This will require some cost of space to accommodate the optical system. Another critical issue would be the development of a photodetector, which has both 2D position sensitivity and good timing resolution.

3.1.3 Aerogel Ring Imaging Čerenkov Counter (endcap)

Introduction

Identification of charged particles over the full kinematic range is one of the basic requirements for the upgraded Belle detector. The RICH, as described in this section, has been designed to separate kaons from pions over most of their momentum spectrum in the forward (endcap) part of the spectrometer,and to provide discriminaton between pions, muon and electrons below 1 GeV/c.

Detector Design Considerations

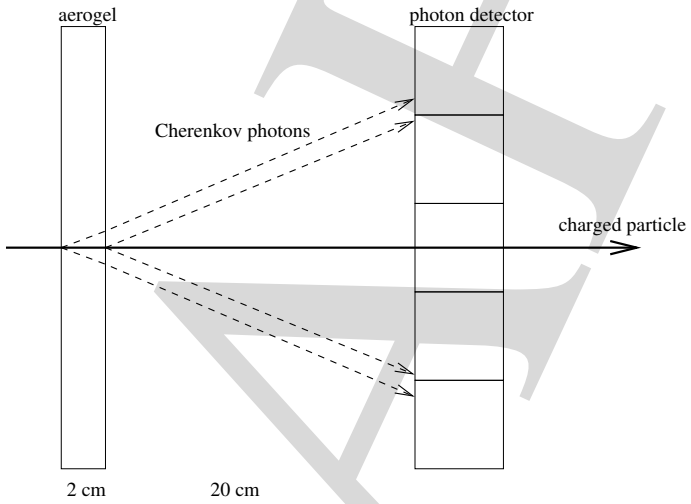

Figure 3.11: *Proximity focusing RICH - principle*

The elements of the proximity focusing RICH counter are (Fig. 3.11):

- a *radiator* where Čerenkov photons are produced by charged particles,
- an *expansion volume* to allow Čerenkov photons to form rings on the photon detector surface,
- an array of *vacuum based position sensitive photon detectors*, that is capable of detecting single photons in a high magnetic field with high efficiency and with good resolution in two dimensions, and
- a *photon detector read-out system*.

The design choices are governed by the following criteria and boundary conditions:

- To achieve the necessary performance, enough photons (about 10) have to be detected for each ring image at least for one of the particle species. This requirement fixes the length of the aerogel radiator to a few centimeters.
- The space allocated to the device in the endcap area is 28 cm in depth.

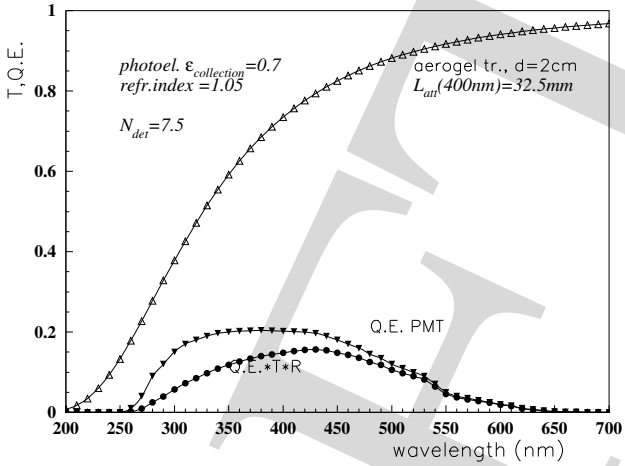

Figure 3.12: *Transmission curve for the aerogel radiator (2 cm) [18] and the quantum efficiency of a typical multi-alkali PMT (H8500 [17]).*

- The required resolution in the measurement of the Čerenkov angle with such a photon detector is only achievable if the expansion gap is at about 20 cm, and the radiator thickness does not exceed a few centimeters, while the photon detector granularity is at about a few milimeters.

Radiator

The Čerenkov radiator is aerogel, a material which is already used in the present Belle ACC (Aerogel Cherenkov Counter). A plane with 2 cm thick radiator tiles is mounted perpendicularly to the beam direction. This radiator was chosen since it combines low mass, a low Čerenkov threshold, and a low dispersion. For aerogel with refractive index $n = 1.05$ the Čerenkov threshold momenta for pions is at 0.63 GeV/c, and the Čerenkov angle corresponding to $\beta = 1$ particles amounts to $\theta_c = 310\,\mathrm{mrad}$. At 4 GeV/$c$, pions and kaons are separated by 23 mrad.

In Fig. 3.12 the transmission curve is shown for a typical 2 cm thick radiator sample. Since the losses of photons are dominated by Rayleigh scattering with a strong wavelength dependence (λ^{-4}) of the attenuation length Λ, the transmission varies considerably over the sensitive interval of a typical bi-alkali photocathode.

The optimal radiator thickness was determined by ploting in Fig. 3.13 the figure of merit, resolution in Cherenkov angle measurement per track,

$$\sigma_\theta^{\mathrm{track}} = \frac{\sigma_\theta}{\sqrt{N_{pe}}},$$

which depends both on the resolution in Cherenkov angle measurement by a single photon σ_θ and on the number of detected photons N_{pe} (c.f. the R&D subsection, Fig. 3.21). The position of the minimum depends slightly on the transmission length. For a typical value of $\Lambda(400\ \mathrm{nm}) = 30$ mm, the best performance is achieved if the radiator thickness is around 20 mm.

Two possible tiling schemes of the aerogel radiator are shown in Fig. 3.14. One of the advantages of the hexagonal scheme is that the fraction of surface where the photon yield

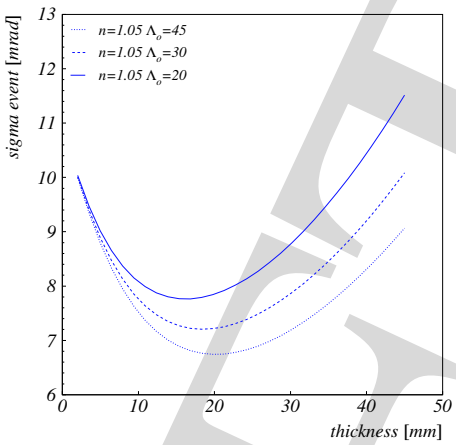

Figure 3.13: *Čerenkov angle resolution per track* $\sigma_\theta^{\text{track}}$ *as a function of the radiator thickness for three different attenuation lengths.*

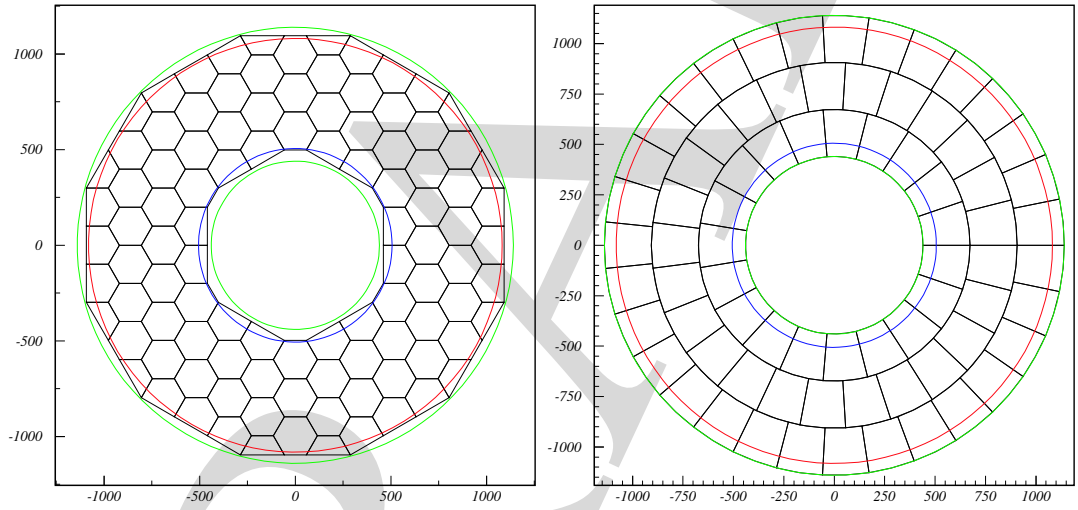

Figure 3.14: *Two aerogel radiator tiling schemes.*

gets reduced due to tile edge effects is smaller (see Fig. 3.22). The hexagonal tiling needs three different tiles (full hexagon with 125 mm sides and two half-hexagons). The tiling with distorted squares needs three different tiles (one for each annulus), with a maximal side of about 220 mm.

Photon Detector

The position sensitive photon detector covers a surface of rougly 3.5 m^2, and is an essential component of the counter. The requirements for the photon detector are summarized as follows:

- Should be immune to the 1.5 T magnetic field,
- Should have single-photon sensitivity with a good single photon peak-to-valley ratio and high detection efficiency,
- Should have position resolution (RMS) of less than 2 mm,

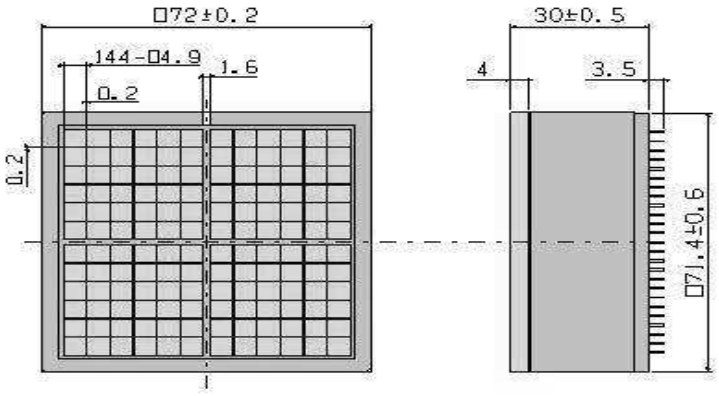

Figure 3.15: *Schematics of the proximity focusing hybrid photon detector (HPD) under development.*

- Should have high sensitivity for photons of $\lambda \approx 400$ nm (c.f. Fig. 3.12).

Currently we consider a proximity-focusing-type Hybrid Photo-Diode (HPD) or a Hybrid-Avalanche-Photo-Diode (HAPD) as the best candidate, since they have both excellent single-photon resolution and high detection efficiency even in high magnetic field. Some kinds of HPD's are already commercially available [14]. However, we can not use a focusing type HPD in the high magnetic field, and the effective area of the currently available proximity focusing type HPD is less than 50%. In order to enlarge the detection area of an HPD, we decided to develop with Hamamatsu Photonics K.K. (HPK) a new HPD of a proximity focusing type with pixel size of 5 mm square. Fig. 3.15 shows a schematic drawing of the H(A)PD, which has a housing of 72x72 mm^2 and 59x59 mm^2 sensitive area. This means 67% of the total area is covered by photo-diodes (PD) or avalanche PDs (APD). Four PD's or APD's, each with a 6x6 pixel array, are installed in a ceramic vessel as shown in Fig. 3.15, which leads to 12x12 pixels in total. The window is made of quartz and the photocathode material is multi-alkali.

A possible tiling scheme of the photon detector surface is shown in Fig. 3.16. The detector surface is covered with 600 HPD PMTs, with a 92% coverage.

Read-Out System

In parallel to the development of the photon detector, we are developing the readout electronics. Since the number of readout channels amounts in total to 86400, we need a special read-out scheme to treat them. We have therefore developed an ASIC which has the following properties:

a) High gain with short shaping times, 5V/pC and 150 ns,

b) Variable gain amp to adjust the threshold, x 1-16,

c) Pipeline readout scheme with shift register,

d) Low power consumption, 5 mW/ch.

A schematic of the ASIC and a photo through microscope are shown in Fig. 3.17. Only the on/off information after the comparator are registered in the shift register. When a trigger

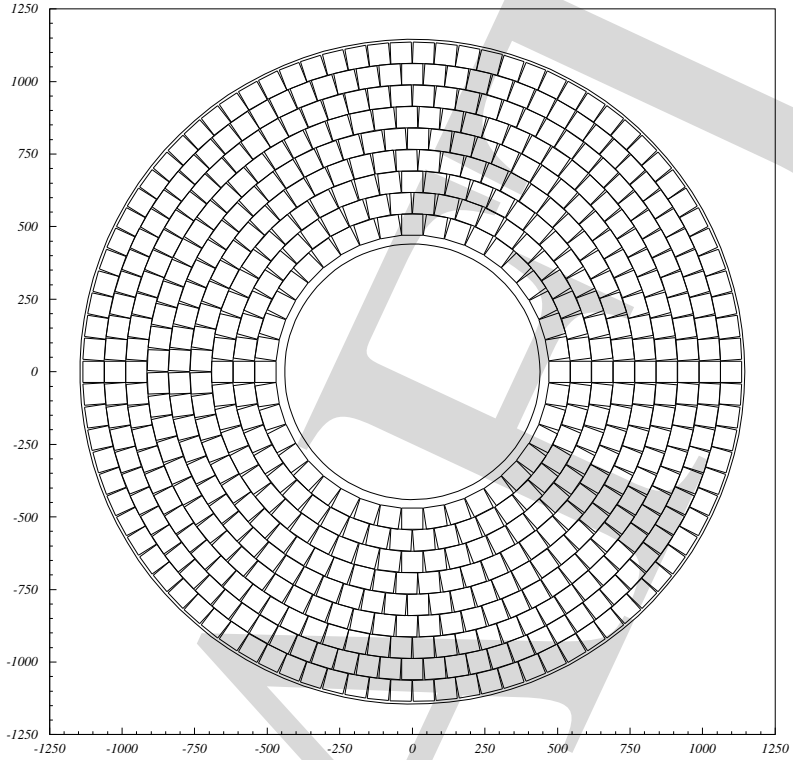

Figure 3.16: *Photon detector tiling scheme.*

signal is accepted, the last 4 bits of the shift register are duplicated in a 4-bits register, which is read out serially.

As a fall-back solution we could employ a low noise read-out system based on the type used in the Belle silicon vertex detector (SVD), but adapted to the special needs of a single photon detector with pads. The system, an upgrade of the integrated circuit used in the CleoIII RICH [23], employs two chips, VA64tap with preamplifiers, amplifiers and discriminators for 64 channels, and LS64 with a 64 channel logic level adaptor stage [24]. The full read-out chain of the chip could be designed in a very similar way as for the read-out for the SVD2 counter.

Expected performance

Number of photons The expected number of Čerenkov photons was calculated by combining the measured values for quantum efficiency $\epsilon_q(\lambda)$ [17] and aerogel transmission $T(\lambda)$ (Fig. 3.12),

$$N_{phot} = 370\text{cm}^{-1}\ d\ \epsilon_e\ \epsilon_a\ \epsilon_t\ \sin^2\theta_c \int \epsilon_q(\lambda)\ T(\lambda)\ \lambda^{-2}\ d\lambda, \tag{3.3}$$

where d is the radiator thickness (2 cm), ϵ_e is the single photo-electron pulse detection efficiency (estimated to be 0.70 for the HPD), and ϵ_a is the active surface fraction of the photon detector surface (0.67 in the case of HPD); $\epsilon_t = 0.92$ is the fraction of the surface covered with photon

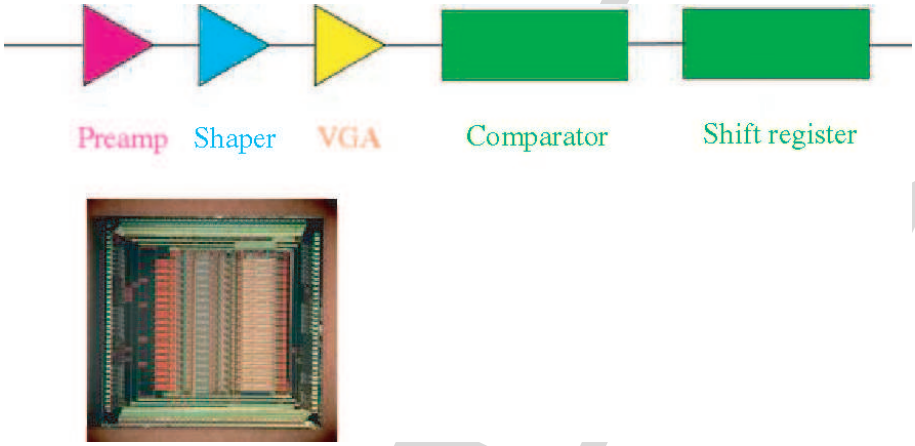

Figure 3.17: *Schematic and photo of the ASIC (4.9x4.9 mm^2).*

detector modules in a particular tiling scheme (Fig. 3.16). The resulting expected number of detected Čerenkov photons is 7.5.

Resolution of the RICH From the photon hit coordinate as measured by the photon detector and from the particle trajectory as given by the tracking chamber, the photon direction is reconstructed to obtain the Čerenkov angle and thus the velocity βc of the particle. Sources of error in the measurement by a single photon are as follows. The finite radiator thickness, $d = 2$ cm, contributes $\sigma_\theta^{emp} = d/(\ell\sqrt{12})\sin\theta_c\cos\theta_c = 8.4$ mrad. The second contribution comes from the finite coordinate resolution of the photon detector $\sigma_\theta^{pix} = a/(\ell\sqrt{12})\cos^2\theta_c = 6.4$ mrad, with a pad size of $a = 4.9$ mm and the radiator to photon detector distance of $\ell = 20$ cm. The chromatic error, a consequence of dispersion, the variation of the refractive index over the energy range of those Čerenkov photons that are detected by the photon detector, is determined from the measured variation of refractive index with wavelength, the transmission of aerogel and the photo-detector quantum efficiency (Fig. 3.12). From the resulting R.M.S. spread σ_n in refractive index we calculate $\sigma_\theta^{dis} = \sigma_n/(n\tan\theta_c) = 2?$ mrad . From the experience with the HERMES RICH [11] we conclude that the contribution due to the imperfections and inhomogenuity of the radiator can be estimated at 2 mrad. Finally, the contribution arising from the error in track parameters as determined by the tracking system and extrapolated to the radiator is expected to amount to $\sigma_\theta^{tr} = 5$ mrad$/(p/\mathrm{GeV}/c)$.

The combined single photon error is finally obtained by summing the above errors in squares. For 4 GeV/c momentum tracks it amounts to $\sigma_\theta = 11$ mrad. Assuming 7.5 detected photons for a $\beta = 1$ particle, the measurement precision is

$$\sigma_\theta^{(N)} = \frac{\sigma_\theta}{\sqrt{N}} = 4 \text{ mrad}. \tag{3.4}$$

In absence of backgrounds, the proposed counter would thus enable a 5σ pion-kaon separation at the kinematic limit of 4 GeV/c. Pions would be separated at a 4σ level from electrons up to about 1 GeV/c.

Background Since the number of photons per ring is rather low, backgrounds could degrade the performance as discussed above. The following sources of background expected in the RICH photon detector were considered:

1. Rayleigh scattered Čerenkov photons from the same track.

2. Čerenkov photons emitted by the same track in the photon detector window.

3. Čerenkov photons emitted by other charged tracks in the event.

4. Čerenkov photons emitted by products of primary photon conversion in the material in front of the RICH radiator and in the radiator itself.

5. Beam related background hits.

6. Electronic noise.

The levels of backgrounds (1) and (2) were estimated from the test beam data (c.f. the R&D subsection, Fig. 3.20a), and turned out to be the dominant source.

The levels of backgrounds (3) and (4) were studied by computer simulation. Because of a rather small diameter of Čerenkov rings (12 cm) as compared to the typicall distance between track impact points on the aerogel radiator, the background (3) does not contribute significantly.

The level of source (5) was estimated from the current background rate in the endcap ACC, and scaled by a factor of 20 as expected from the luminosity increase. This rough estimate yields values from 60 Hz/cm^2 to 140 Hz/cm^2 for the modules at the maximum and minimum radial distance from the beam. Finally, the electronic noise is estimated by assuming a conservative value of 10^{-3} for the probability of a noise hit.

In total, we expect 0.7 smoothly distributed background hits within the annulus of $\pm 3\sigma_\theta$ of the 4 GeV/c pion ring.

Particle identification capabilities The particle identification capabilities of the counter were evaluated by using simulated data. The backgrounds which are not included in simulation (sources 1,2,5,6) were generated according to observed or expected rates.

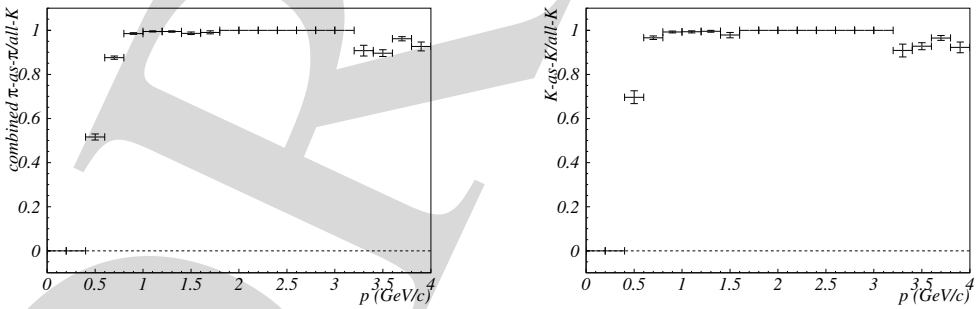

Figure 3.18: *Particle identification capabilities of the aerogel RICH counter: pion identification efficiencies at 5% kaon misidentification probability (left); kaon efficiency at 5% pion misidentification probability (right).*

R&D Results

Aerogel radiator The hydrophobic aerogel with a low refractive index ($n = 1.01 \sim 1.03$), as developed for the Belle-ACC, is characterized by a high transmission length (~ 40 mm at a wave length of 400 nm). However, the transmission length of aerogel with a higher refractive index of $n = 1.05$ fell below one half the value compared to the aerogel with $n = 1.03$. Keeping in mind that for a collider experiment a hydrophobic aerogel is preferred to a hydrophilic one, we reexamined the hydrophobic aerogel production technique in a joint development with Matsushita Electric Works Ltd.

As a result, we found that the important factors determining the transmission length are the solvent and selection of the precursor to be used for its production. Originally, we used methyl-alcohol for the solvent, and methyl-silicate as a precursor [9]. When we applied dimethyl-formamide (DMF) [20], and changed the supplier of the precursor, we could improve considerably the transmission length of the aerogel. Fig. 3.19 shows the refractive indices of

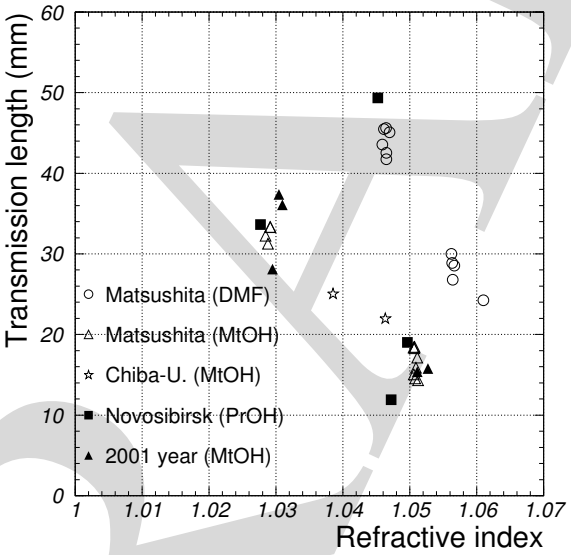

Figure 3.19: *Transmission length at 400 nm and refractive index at 405 nm for the aerogel samples used in the test.*

aerogel and the relation to transmission length for samples which were used in the beam test. The Matsushita(DMF) samples are clearly superior to other hydrophobic aerogels.

System test In a series of beam tests we have checked the performance of a complete system. While in the first test [15] at the KEK-PS $\pi 2$ beam line an array of multi-anode PMTs (Hamamatsu R5900-M16) was used for photo-detection, the recently developed flat-panel PMTs, Hamamatsu H8500, were employed in the second one [16]. 16 PMTs were used in a 4×4 array and aligned with a 52.5 mm pitch, with an effective area of photon detection of 84%. At the back of each PMT, an analog memory board is attached to read out multi-channel PMT signals.

Most of the test measurements were performed with a π^- beam at 3 GeV/c. To systematically evaluate the detector performance, data were taken with different aerogel samples with

various transmission lengths and thicknesses. Data were also taken by varying the π^- momentum in the range from 0.5 GeV/c to 4.0 GeV/c.

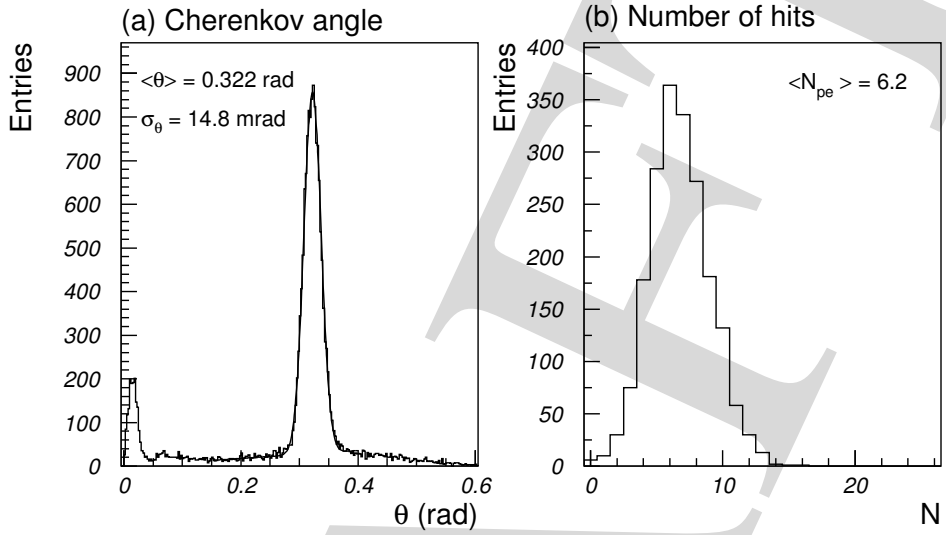

Figure 3.20: *Distribution over the Cherenkov angle for single photons (a), and the number of detected photons per ring (b), for a* 20 *mm thick aerogel radiator sample with* $n = 1.056$ *and a transmission length of* 30 *mm.*

Fig. 3.20a shows a typical distribution of the Cherenkov-angle for single photons. Cherenkov photons from the aerogel radiator are clearly seen with a low background level. The flat background hit distribution on the photon detector is consistent with the assumption that it originates from Cherenkov photons which were Rayleigh scattered in the radiator. The peak at small Cherenkov angles is due to Cherenkov radiation generated by the beam particle in the PMT window.

Cherenkov-angle resolution for single photons The angular resolution was obtained from a fit of the Cherenkov angle distribution (Fig.3.20a) with a Gaussian signal and a linear function for the background. The resolution was typically around 14 mrad, independent of the refractive index. The main contributions to the resolution of the Cherenkov angle come from the uncertainty in the emission point and from the pixel size of the PMT. The measured variation of the resolution with the thickness of aerogel is shown in Fig. 3.21 together with the expectations. The measured resolution matches the expected values reasonably well, appart from a discrepancy between the two, which could be accounted for by a constant additional contribution of about 6 mrad. The discrepancy could arise from the effect of aerogel (non-flat aerogel surface and possible non-uniformities in the refractive index due to position variation and chromatic dispersion), which are subject to further investigation.

Photoelectron yield Fig. 3.20b shows a typical distribution of the number of hits within $\pm 3\sigma$ from the average Cherenkov angle. The number of hits for the signal region was estimated

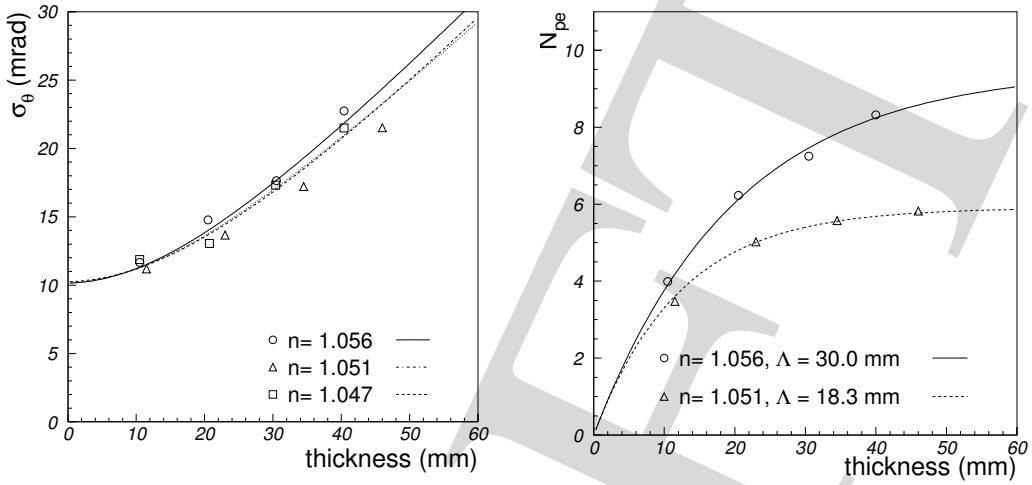

Figure 3.21: *Angular resolution (left) and the number of detected photons per Cherenkov ring as a function of the aerogel thickness. The symbols correspond to the data recorded with different aerogel samples.*

by subtracting the background from the fits to the Cherenkov-angle distribution. Fig. 3.21 shows the dependence of the number of detected photons on the aerogel thickness. As expected, the number of photons does not linearly increase with the aerogel thickness, but saturates due to the scattering effect in aerogel. For pions with momenta above 1 GeV/c, the number of detected Cherenkov photons was typically around 6 for aerogel samples with $n = 1.05$. The deviation from the expected value (about 9) can be accounted for by the rather early development stage of the employed PMT tubes. In fact, if normalized to the best tubes in the second delivery batch, the yield per ring is very close to the expected value.

It has been already noted by the HERMES group [11] that a loss of Cherenkov photons occurs at the side wall boundaries between adjacent aerogel tiles. We have confirmed this finding by measuring the number of photons on the Cherenkov ring as a function of the distance of the charged particle impact point from the boundary between two tiles. The measurement is shown in Fig. 3.22, where a dip is seen at the tile boundaries for two different tiling schemes. In order to eliminate other geometrical factors, like for example the acceptance of the photon detector, the measured yield was normalized to the yield obtained with one tile covering the entire range. The result clearly indicates a reduction of yield when the charged particle is closer than about 5 mm to the boundary of a 2 cm thick aerogel tile. It is worth noting that a simple model, where all photons hitting the boundary between the two tiles get lost, accounts for most of the observed dependence. From the result it is clear that the tile size should be as large as possible to reduce the impact of the loss.

Particle Identification Finally, we estimate the performance of pion/kaon separation in the momentum range of around 4 GeV/c. If we take into account a typical measured value for the single-photon angular resolution, $\sigma_c \sim 14$ mrad, and the number of detected photons $N_{pe} \sim 6$, typical for 20 mm thick aerogel samples with $n = 1.05$, we can estimate the Cherenkov angle resolution per track to be $\sigma_c/\sqrt{N_{pe}} = 5.7$ mrad. This naive estimate is also confirmed by the direct measurement shown in Fig. 3.23. Here, the track-by-track Cherenkov angle is calculated

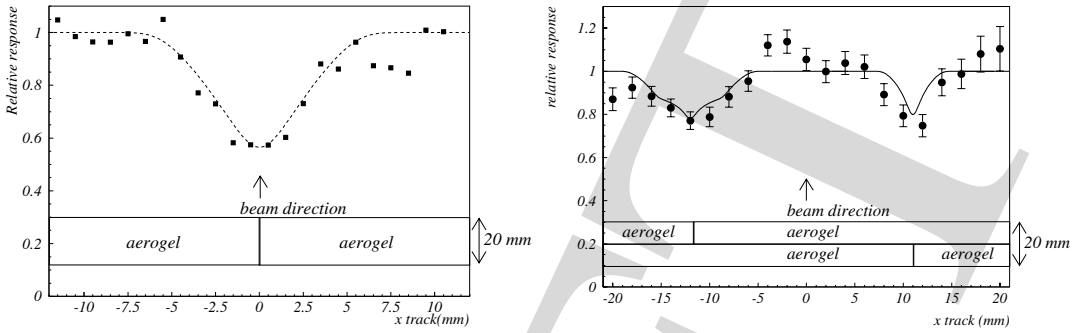

Figure 3.22: *The number of Cherenkov photons detected on the ring, as a function of the charged particle impact point position on the aerogel tile. The values shown are normalized to the measured values in case of a single tile covering the full range. Also shown is the estimate of a simple model.*

by taking the average of the angles measured for hits around the predicted position of the Cherenkov ring. From this we can deduce that at 4 GeV/c, where the difference of Cherenkov angles for pions and kaons is 23 mrad, a 4σ separation between the two is possible. As an additional cross check, we have also collected data with the pion beam of 1.1 GeV/c, which can be used to represent a kaon beam of 4 GeV/c (apart from a slightly larger sigma due to multiple scattering). As can be seen from Fig. 3.23, the two peaks are well separated.

HPD development Although the system test was very successful, there are still several issues which have to be solved for implementation in the Belle spectrometer. The most important item is the development of a PMT which can be operated in a high magnetic field (1.5 T). In order to confirm the ability of candidate photon detectors HPD and HAPD to efficiently detect single photons over a large active area, a single channel HPD and a 3x3 multi-channel HAPD were tested by using a laser diode light pulser ($\lambda = 850$ nm). Fig. 3.24 shows a multi-photon spectrum obtained by a HPD, which was operated at 8 kV for electron bombardment (EB) (typical EB gain was 1500) and 80 V for bias. The leak current was 4 nA and the detector capacitance was 20 pF.

Multi-photon spectrum was obtained also by the HAPD prototype (Fig. 3.25). The gain was higher ($2.6 \cdot 10^4$) in the case of the HAPD due to the avalanche gain of about 15. However, the detector capacitance was 73 pF and the leak current amounted to 14 nA, resulting in a worse signal to noise ratio than in the case of the HPD. Although both the HPD and the HAPD have shown an excellent performance, the HPD gives a slightly better resolution.

Prototype production of APD's and PD's is going on in HPK, and evaluation of the samples is being carried out. While so far there are no serious problems for the PD's except for a slightly worse timing response, a large leak current was observed in APD's after the activation of photocathode. Futhermore larger noise than expected is seen in APD's. Hamamatsu Photonics is investigating the HAPD's to solve this problem in the next batch. A delivery of prototype 12x12 channel HAPD's is expected in January 2004, and a beam test is planned for February.

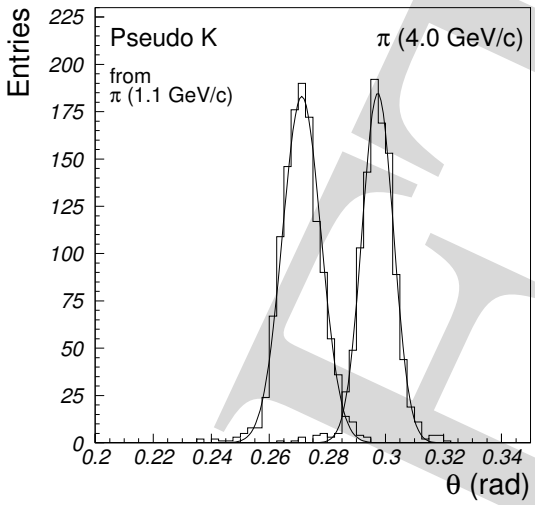

Figure 3.23: *Cherenkov angle per track for pions of* 4.0 GeV/c *and* 1.1 GeV/c. *Pions at* 1.1 GeV/c *are used to represent the kaon beam of* 4 GeV/c. *The angular resolutions for* 4.0 GeV/c *and* 1.1 GeV/c *are* 5.4 *mrad and* 6.7 *mrad and two peaks are separated by* 4.2σ.

3.1.4 Other possibilities

10ps TOF

In order to obtain higher PID power, we are studying on a very-high-resolution time-of-flight (TOF) counter. The point of this TOF counter is to use Cerenkov lights radiated in a small crystal block. For a practical use, these counters set as tiles in the current TOF region.

Test counter

We have studied the simple test-counter, whose design is shown in Fig. 3.26. Charged particles go through the quartz block and the photo-detector. To improve the time resolution, we implement the following feature: (1) Instead of scintillation light, Cerenkov light is used because the emission time is negligibly small. (2) A small size radiator is used in order to reduce the time spread of the internal reflecting photons, which is due to the propagation length spread and the chromatic dispersion of the light velocity. (3) The high-resolution photo-tube whose transit-time-spread (TTS) is $\sigma_{\rm TTS} = 50 \sim 100$ ps for a single photo-electron is used. Such a photo-tube gives the good performance, even though the number of Cerenkov photons are much smaller ($100 \sim 200$ photo-electrons) compared to scintillation lights. In a simulation study, the expected time resolution is less than 10 ps.

We carried out a beam-test at the π2-line of the KEK-PS at December 2002. The two types of photo-multiplier-tubes, L16-PMT(HPK R5900U-00-L16) and MCP-PMT (HPK R3809U-50-25X), are tested. The purpose of the beam-test is to confirm the performance. To evaluate the time resolution, we put two same counters along the beam direction and measure the residual of detected time between the up-stream and down-stream counters.

The L16-PMT is the metal-packaged line-focus-type PMT with 16 channel anode. The TTS for each channel is $\sigma_{\rm TTS} \sim 75$ ps for a single photo-electron. One advantage of the L16 is that

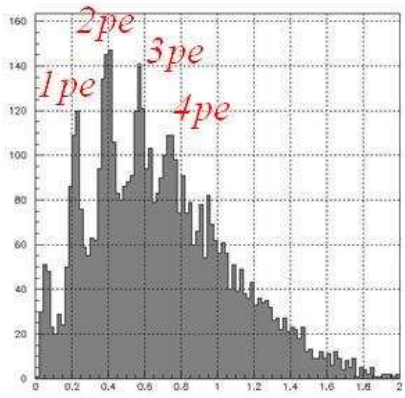

Figure 3.24: *Multi-photon spectrum obtained by the single-channel HPD.*

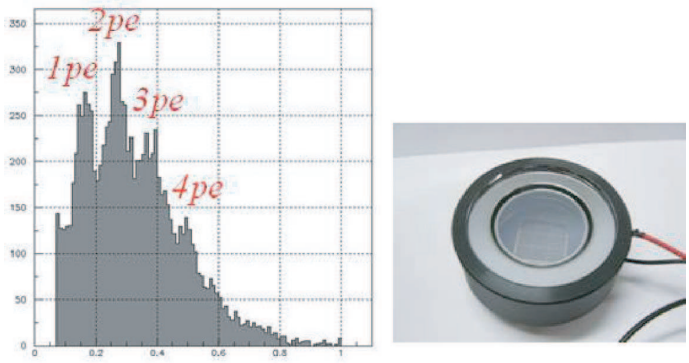

Figure 3.25: *Multi-photon spectrum obtained by the 3x3 multi-channel HAPD and a photo of the HAPD.*

the required time resolution for each channel is not so severe because we can use 16 measured-times. For the L16-PMT, the number of detected photo-electrons is $\sim$ 120 in total and the obtained time-resolution is $\sim$ 30 ps for each channel. By averaging over the 16 channels, the total time-resolution is obtained to be $\sigma_{\mathrm{L16}} = 12.1$ ps.

The MCP-PMT is the single-anode PMT equipped with two micro-channel-plates, whose TTS is $\sigma_{\mathrm{TTS}} \sim 50$ ps for a single photo-electron. For the MCP-PMT, the number of detected photo-electrons is 150 $\sim$ 200 and the obtained resolution is $\sigma_{\mathrm{MCP}} = 10.6$ ps, as shown in Fig. 3.31.

In this beam-test, we have obtained 10.6 ps resolution and confirmed that our idea is correct in principle. For both types, we obtain the number of detected photo-electrons as we expected. However, the time resolution is a little worse than expectation, which is due to the time fluctuation in the readout electronics. The error of the readout system is measured to be $\sigma_{\mathrm{elec}} \sim 9$ ps.

Simulation

Based on the beam-test result and the pulse-laser test result, we have developed some reliable simulation program to make a design with a larger radiator and some different incidence situations. The following conditions are implemented into the simulation:

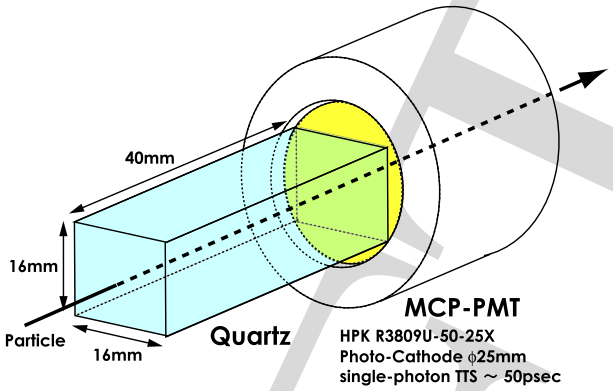

Figure 3.26: Test counter with MCP photo-tube.

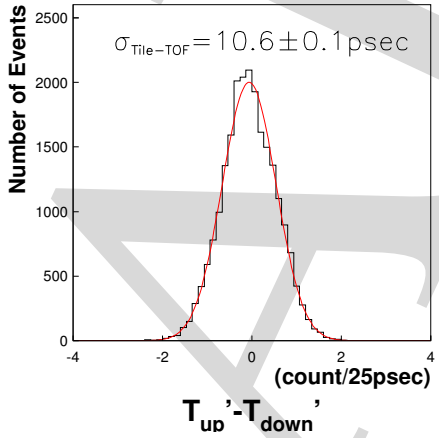

Figure 3.27: TDC residual distribution between the up-stream and down-stream counters for MCP type.

- The number of generated photon is ~ 1900 for 20 mm of path-length and depends on the wavelength λ of Cerenkov light.
- The generated position and direction is as the Cerenkov cone. The Cerenkov angle depends on λ.
- The time offset due to the time-of-flight of incident charged particle and the propagation time of the Cerenkov light in the radiator is considered.
- The chromatic dispersion is applied. (Light velocity in the radiator depends on λ.)
- The quantum efficiency (QE) is ~ 18 %, which is modeled by the measurement shown in Fig. 3.28. The correction efficiency (CE) is 36%.
- The TTS is 50 ps. The time fluctuation follows the Gaussian.
- The pulse shape for single photon and its ADC fluctuation is modeled by the pulse-laser measurement. The implementation of pulse response generates the time-walk effect.

An example of event display is shown in Fig. 3.29. Here, the incident angle and distance from PMT is 45° and 100 mm, respectively. The radiated Cerenkov photons indicated by blue lines propagate in the radiator ($200 \times 100 \times 20$ mm) and reach the PMT. The time distributions of Cerenkov photons are shown in Fig. 3.30. In this case, the number of detected photons is

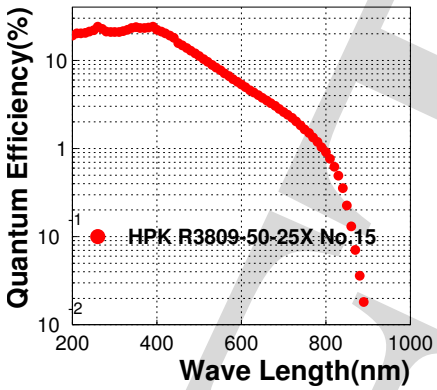

Figure 3.28: Quantum efficiency depending on the light wavelength for the MCP (HPK R3809U-50-25X) measured by HPK.

$\sim$ 116 per event, and the time resolution is $\sim$ 18 ps.

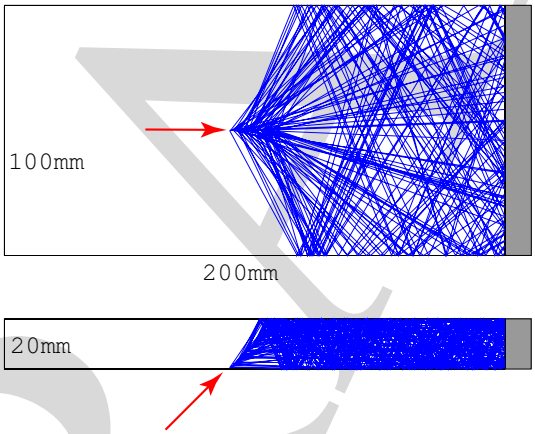

Figure 3.29: One event display. The incident position and direction is indicated by red arrow. Blue lines show the trajectory of Cerenkov photons and gray box shows the PMT.

Conceptual layout

Time resolution is almost determined by the number of photons in the wavefront and it largely depends on the incident angle and incident position (distance from photo-detector). Fig. 3.31 shows the contour plot of the time resolution depending on the incident angle and distance for $\pi^{\pm}$ of $p = 3.0$ GeV/c. The definition of the incident angle and distance is indicated in Fig. 3.32. In the MC studies, there is no significant difference of the time resolution for the momentum of 1.0 $\sim$ 4.0 GeV/c at least. The contour plot shows the good time-resolution when the incident angle is small and the distance is short. However, it is hard to reach the 10 ps resolution for wide acceptance using this radiator shape.

If we decide to keep the time resolution to be $<$ 20 ps, the length of the radiator l can be expressed as a linear function of incident angle α by $l(\mathrm{mm}) = 4 \times (90^\circ - \alpha(\mathrm{degree})) + 20$. Because the incident angle directly depends on the polar angle θ of a incident particle, the relation between θ and l is expressed by $\theta(\mathrm{degree}) = 90^\circ + \tan^{-1}\left(\frac{20}{l}\right) - \frac{l-20}{4}$, where the unit of l is mm and the thickness of the radiator is 20 mm. Following this relation, we can draw the

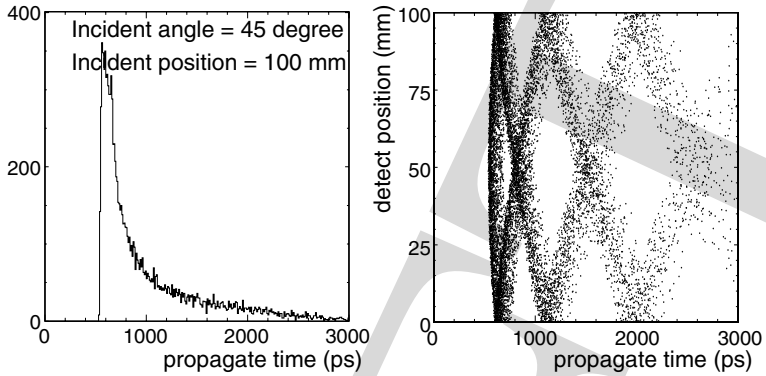

Figure 3.30: Propagation-time distribution (left) and its dependence on the detected position on the PMT (right).

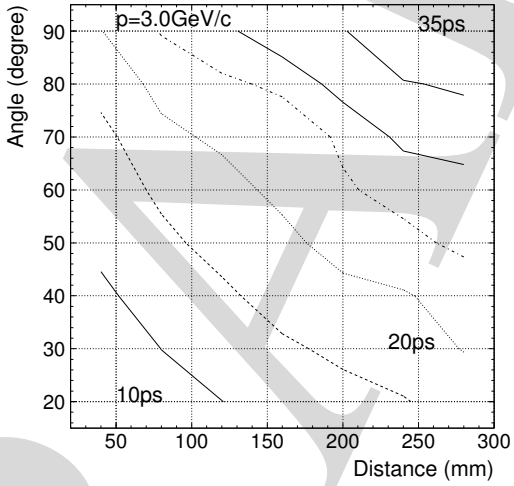

Figure 3.31: Contour plot of the time resolution depending on the incident angle and distance for $\pi^{\pm}$ of $p = 3.0$ GeV/c.

conceptual layout as Fig. 3.33. In order to keep the 20 ps resolution for all region, the radiator length change gradually depending on the z-position.

The point of this detector is summarized in the following:

- A small Cerenkov radiator and high resolution PMT is used.
- There is a robustness against the high hit-rate (background-rate) because of the small acceptance per counter.
- The existing technologies (Quartz and MCP-PMT) are used.
- Many trigger topologies can be formed.
- There is room for optimization of radiator shape because the incident angle is limited due to the small acceptance.

Next R&D items are 1) to make a test counter with larger radiator in order to confirm the simulation result, 2) to design a optimized shape and 3) to develop a very-high-resolution readout system. The PMT with large effective acceptance is also one of next R&D items, but

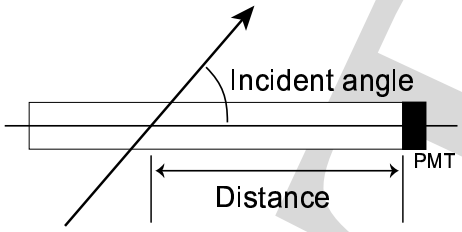

Figure 3.32: Definition of incident angle and distance.

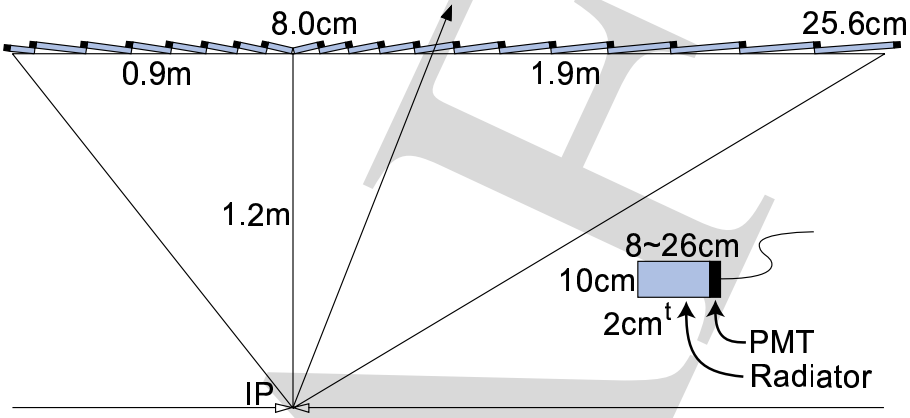

Figure 3.33: Conceptual layout of tile TOF.

it coincide with the TOP R&D.

50ps TOF

Conceptual design of 50 ps TOF counter

The design of 50 ps TOF is based on the performance of the present TOF system for Belle detector, which has achieved 100 ps time resolution, and provides 3σ π/K separation upto 1.2 GeV/c.

The present Belle TOF system consists of 128 scintillation (BC408) counters of 6cm width, 4 cm thickness and 255cm length aligned on a barrel of 1.2m in radius. Each TOF counter is viewed at the both ends by R6680 PMTs. This system is working at a high luminosity of $10^{34}/\mathrm{cm}^2/\mathrm{s}$ with an efficiency of better than 90%.

It is also providing a fast event timing in online with a precision of 2 ns, that helps T0 determination for the tracking chamber and other subdetectors. In offline analysis, the TOF hit timings are used to determine the event timing with a precision of 0.5 ns for track reconstruction.

Figure 3.34 shows the time resolution as a function of z position for a prototype of Belle TOF counter, which was measured in the beam test in 1996. The intrinsic resolution of a typical counter was obtained to be 80 ps at the center of the counter.

From this test result, we can design 50ps TOF system with a fine segmentaion along z-direction. Figure 3.35 shows the conceptual design. One TOF counter of 255 cm length is devided into three counters of 100 cm length. We except an intrinsic time resolution of 50 ps by assuming that it is scaled with square root of the counter length. Beam test of BC408 and BC404 should be done to confirm this design.

The major background to TOF counter is caused by spent electrons and positrons in the

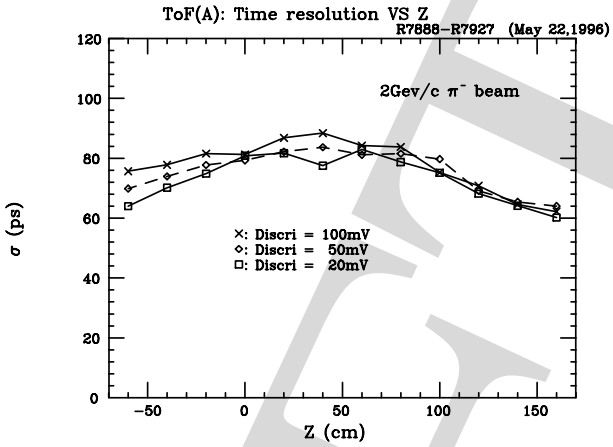

Figure 3.34: Time resolution of present Belle TOF.

ring, which hit the beam pipe and masks in the interaction region to generates electromagnetic showers. The photons intercating inside TOF counter gives a high signal rate of small sigals. In the present TOF system, we have 12 cm wide and 5 mm thick scintillation counters (TSC) in front of TOF counter with 15 mm separation. The coincidence between the TOF and TSC can eliminate a signal rate due to photon interaction in TOF counters. The rate reduction is about a factor 3.

The short counter can reduce the signal rate, propotionally to the counter length. In the 50 ps TOF design, we have two layers of 6 cm wide and 2.5 mm thick TSC at inner and outer sides of the TOF counters. As the separation gap is about 4 cm, we expect a larger reduction of the photon background rate. Table 3.3 indicates the counter dimensions. The material thickness of TOF and TSC counters is the same as the present TOF system, which is 11% in radiation length. This design requires 110 mm in radial space, that conflicts the space allocated for the present TOF system (80 mm).

Table 3.3: 50 ps TOF configuration.

Counter	Scini.	W × T × L (cm)	Seg.($\phi \times Z$)	PMTs
TOF	BC408/BC404	$6 \times 4 \times 100$	128×3	×2
TSC(inner)	BC412	$6 \times 0.25 \times 260$	128×1	×1
TSC(outer)	BC412	$6 \times 0.25 \times 260$	128×1	×1

PID capability

Figure 3.36 shows σ π/K sepraration capability with TOF and CDC dE/dx measutrement. It is stressed that 25 ps TOF and 4% dE/dx can cover almost all momentum region with more tna 3σ separation. 50 ps TOF with 6% dE/dx only provides 2σ separation at higher momentum above 2 GeV/c. If 50ps TOF could coexist with the present ACC, this design is one of the backup options.

System error for precise TOF measurement

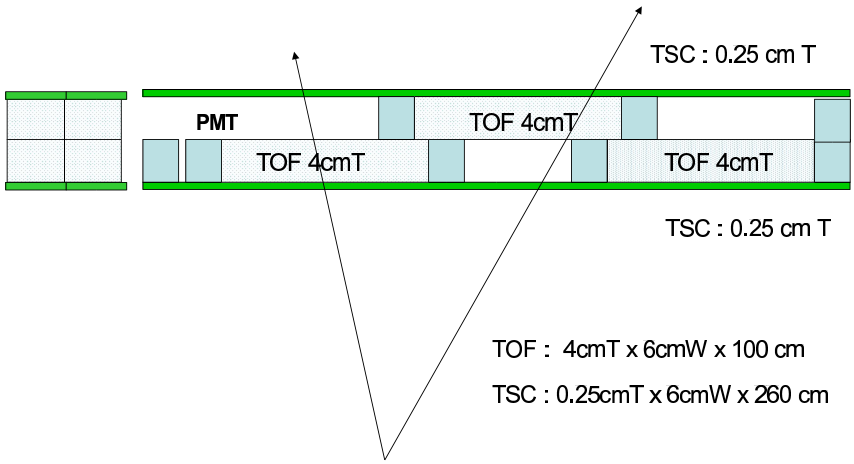

Figure 3.35: Conceptual design of 50 ps TOF

In the present TOF system, we have a systematic error of 50ps in the readout, which is considered as follows.

1. *Time jitter in beam collision;* A beam size of 7 mm corresponds to 20 ps. There may be an additional jitter of a few ps in variation of beam phase to RF clock for each bunch.

2. *Readout errors in time stretcher;* We found an error of 20 ps in a bench test of the time stretcher.

3. *Discriminator and ground level noise;* As we are using preamp of 5 times, the time jitter in discriminator is less than the ground level noise. We observed 5 mV ground level noise and set the dscrimination level at 50 mV. We guess the error to be 10 to 20 ps.

4. *Error in time walk calibration;* We have an error in time walk calibration, which matchs the TOF measured timings to those expected from tracking. The calibration includes tracking systematics too. An error of path length of 6 mm in tracking corresponds to 20 ps. Also assumption of the TWC calibraion function also gives some systematics. From the maximum deviation of the data and expected TOF after calibration, we guess a total error of 30ps for the time walk correction, including the errors due to tracking.

5. *Particle and momentum depedence;* We are making emperical correction to match the data to the predicted one using a large data sample. It is dependent on tracking code itself, in particular at low momentum, while it is not essential to separate π/K at higher momentum.

To achieve 50 ps, we need to reduce those systematics errors to less than 20 ps in total.

Estimation of TOF rate and requirement of fast readout system

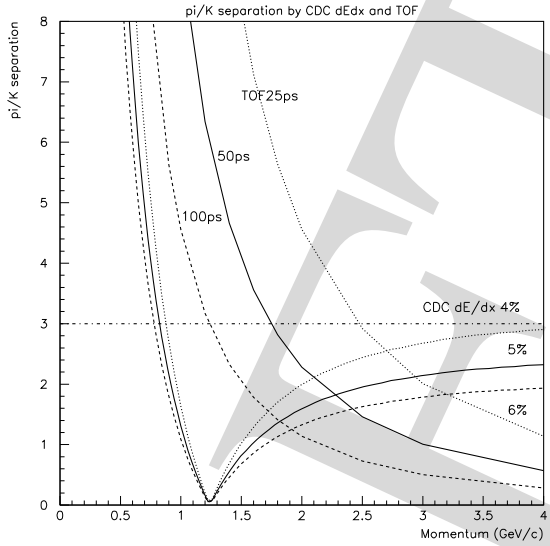

Figure 3.36: π/K sepration with TOF and cdc dE/dx.

Table 3.4 shows TOF rates and hit efficiencies for various cases, which are estimaded using the data in exp27. The norminal threshold is set to 0.2-0.25 mips, which corresponds to about 2 MeV of energy loss in a TOF scitillator. The energy loss in 4 cm thick TOF is 8 MeV and varies on crossing angle. The inefficiency of TOF hits is found to be 3% in the data at the luminosity of 10^{34}. Although the present readout is using MQT for Q and time stretcher for T with 600 ns dead time which had been developed ten years ago, they are not fast enough for the higher bavkground.

With the 1m TOF counters (3TOF opt.) and fast readout, we can keep the TOF hit efficieny less than a few %. It is essential to develop fast readout for T and Q measurements with 100 ns or shorter dead time. Design discussion on the fast readout system should be made somewhere else in this report.

Table 3.4: TOF hit efficiency at a luminosity of 10^{35} for various assumptions.

L ($cm^{-2}s^{-1}$)	$I_{HER}(A)$ $\times I_{LER}(A)$	Background assumption	Rate(KHz)/Ineff(%) w/ 1-TOF opt.	3-TOF opt.	Ineff(%) w/ 100ns elec.
10^{34}	1×1.5	exp27	44/3		
10^{35}	4×6	$\propto (I_{HER} + I_{LER})$	174/12	58/4	
10^{35}		$10 \times L$	440/30	147/10	2-3
10^{35}		$20 \times L$	880/60	293/20	3-4

References

[1] M.Akatsu et al., Nucl. Instr. Meth. A **440**, 124 (2000); T.Ohshima, ICFA Instrum. Bull. 20, 2 (2000); T.Ohshima, Nucl. Instr. Meth. A **453**, 331 (2000).

[2] B. Aubert *et al.* (BaBar Collaboration), Nucl. Inst. Meth. A **479**, 54 (2002);

[3] M.Hirose et al., Nucl. Instr. Meth. A **460**, 326 (2001).

[4] Talks presented by K.Inami and also by A.Drutskoy at the Super B Factory Workshop in Hawaii (2004).

[5] M.Cantin et al. Nucl. Instr. Meth. **118** (1974) 177.

[6] A.Abashian et al., Nucl. Instr. and Meth. A **479** (2002) 117.

[7] T.Sumiyoshi et al., Nucl. Instr. and Meth. A **433** (1999) 385.

[8] T.Iijima et al., Nucl. Instr. and Meth. A **453** (2000) 321.

[9] I. Adachi et al., Nucl. Instr. and Meth. A **355** (1995) 390390; T. Sumiyoshi et al., J. Non-Cryst. Solids **225** (1998) 369.

[10] D.E.Fields et al. Nucl. Instr. Meth. A **349** (1994) 431.

[11] N.Akopov et al. Nucl. Instr. Meth. A **479**(2002) 511.

[12] T.Ypsilantis and J.Seguinot, Nucl. Instr. Meth. A **368** (1995) 229.

[13] T.Iijima, "Aerogel Cherenkov Counter in Imaging Mode", JPS Meeting, Tokyo Metropolitan University, September 1997.

[14] DEP catalog

[15] I. Adachi et al., "Test of a proximity focusing RICH with aerogel as radiator", Proceedings for the IEEE Nuclear Science Symposium, Norfolk, VA, November 10-15, 2002; hep-ex/0303038; T.Iijima et al., Nucl. Instr. Meth. A **502** (2003) 231.

[16] T. Matsumoto et al., to be published in NIM A; physics/0309032.

[17] H8500 data sheet, Hamamatsu Photonics K.K.

[18] aerogel transmission

[19] Hamamatsu Photonics K.K.

[20] Matsushita Electric Works Ltd. has a Japanese patent (No. 2659155) for usage of DMF as solvent to make aerogel.

[21] A.R. Buzykaev et al. , Nucl. Instr. Meth. A **433** (1999) 396.

[22] H.Ikeda et al., Nucl. Instr. Meth. A **372** (1996) 125.

[23] M. Artuso et al., Nucl. Instr. Meth. A **502** (2003) 91.

[24] Ideas SA, Oslo.